Institute of Space and Aeronautical Science, University of Tokyo
Report No. 457, December 1970

The Interaction between a Plasma Flow and a Magnetic Nozzle with Strong Hall Effect

By

Osami OKADA* and Kyoichi KURIKI

Summary: An experimental research on the interaction between a plasma flow and a magnetic field with nozzle-shaped lines of force was made with a large electron Hall parameter. The experiment was made using the plasma flow from a dc arc discharge and a magnetic field generated by a current loop. Measurements were made of the radiation emerging from the plasma flow, the number density of ions, the electron temperature, the impact pressure and the velocity of ions. The results showed that by the application of the magnetic field, the flow was strongly channelled and the electric field was induced in the flow. A theoretical analysis was made to explain the experimental results, using the gasdynamic equations, the generalized Ohm's law and the Maxwell's equations. The theoretical results explained very well the mechanism of the interaction occuring upstream of the coil. The plasma flow was found to flow along magnetic lines of force. The magnetic nozzle, however, accelerated the ions to a higher velocity than that expected from the isentropic expansion.

CONTENTS

* Central Research Laboratory, Hitachi Ltd.

I. Introduction

The interaction between a plasma flow and a magnetic field has been a fascinating subject for many investigators in relation to the space propulsion, to the thermonuclear fusion and to the MHD power generation. For the purpose of the production and the containment of a dense and hot plasma for the controlled thermonuclear fusion, the confinement by the magnetic field is indispensable and the mechanism of the interaction between the magnetic field and plasma needs be clarified. The acceleration of a plasma to a high speed is the basic requirement to obtain a high specific impulse for a space flight. The existence of a magnetic field is effective to transform the thermal energy to the energy of a directed motion.

In the most of the devices which have been proposed for the above applications, such as the mirror and the cusp fields, the MPD (Magnetoplasmadynamic) arc thruster and the travelling magnetic field accelerator, an important problem is the interaction of a plasma flow with a spatially varying and axisymmetric magnetic field. Our interest is restricted to the interaction between the plasma flow and the external magnetic field with the converging-diverging field lines, the magnetic nozzle.

The collisions of the charged particles are expected to have a strong effect on the interaction pattern. When a tenuous plasma of negligible collisions is considered, the interaction is mostly explained in terms of the particle motion in the magnetic field. Along the diverging lines of force, the energy of a gyrating particle is transformed into the energy of directed motion, and an example in the mirror field is shown by Spitzer [*1*]. The experimental work in this regime was conducted by Kosmahl [*2*], in which the microwave heating was made at the throat of a magnetic nozzle and the divergence of the plasma flow was investigated. He also calculated the particle trajectories considering an electrostatic force between electrons and ions. Then he compared the calculated trajectory with the experi-

mentally obtained boundary of the luminous jet, and showed a good agreement.

In a denser plasma, the Hall current must be considered. When the ratio of the electron gyration frequency to the collision frequency, which is called the Hall parameter of electrons, is not negligible compared to unity, there result the Hall current and potential. In the magnetic nozzle with an axial symmetry, the azimuthal current is caused by the Lorentz interaction, namely, by the interaction of the axial motion of charged particles with the magnetic field. The interaction between the magnetic field and the azimuthal current produces the Hall current in the plane including the axis of symmetry.

The interaction of the one-dimensional plasma flow with magnetic nozzle generated by a current loop was investigated theoretically by Hasimoto [*3*]. In his analysis, the macroscopic MHD equations, generalized Ohm's law and the Maxwell's equations were used and the expansion was made assuming the Hall parameter, the magnetic Reynolds number and the interaction parameter to be sufficiently small. The resulting pattern of Hall current seems to be consistent with the qualitative exceptation of the interaction. Otis [*4*] made an experimental and theoretical investigation of the interaction between a plasma jet and a magnetic field in nearly the same configuration as that of Hasimoto. Otis solved the Maxwell's equations and the generalized Ohm's law under the assumption of a small Hall parameter. Using an approximate magnetic field distribution, the Hall current pattern of nearly the same as that of Hasimoto was obtained. Otis also calculated the perturbation on the flow field from the macroscopic equations of motion with the neglection of the Hall effect. The experimental results in his report, however, are mostly for the Hall parameter larger than unity and do not include the measurement of the flow field.

The so-called MPD thrustor which is composed of an arc discharge and a diverging magnetic field applied on the discharge region, has been developed for the purpose of a space propulsion. Quite promising results such as a high flow velocity, a high thrust density and a high efficiency are reported. The Hall parameter estimated from the reported results is larger than unity. Clark and Jahn [*5*] in their survey report discussed the mechanism of the acceleration in terms of blowing and pumping effects due to the electromagnetic force and of an electro-thermal contribution, the original function of the arc jet. But the mechanism of acceleration is not fully clarified. The application of a magnetic field in the discharge region makes it very difficult to discuss the mechanisms of the acceleration separately. Therefore, the investigation of a magnetic-nozzle flow will isolate the one of the plasma-acceleration mechanisms of the MPD thrustor.

In spite of the fact that theoretical works on the flow interacting with magnetic nozzle already published are mostly concerned with the case of small Hall parameter, the knowledge of the interaction at large Hall parameter is required from the practical view point. With reference to the generalized Ohm's law, the induced current decreases as the Hall parameter increases. The interaction parameter, on the other hand, is propartional to B^2. Then the increase of the magnetic field brings two effect, the decrease of the Hall current and the increase of the inter-

action. Otis observed that the deformation of the flow boundary increase as the magnetic field is intensified, but the detailed investigation on the interaction at a large Hall parameter has not yet been made.

The purpose of the present investigation is to clarify the mechanism of the interaction between a plasma flow and an applied magnetic field with nozzle-shaped lines of force when the Hall parameter of electrons much exceeds unity. Experiments were performed with an arc plasma jet and a magnetic nozzle generated by the current through a ring coil.

In Chapter II the experimental apparatus is explained. The description of an arc-heated plasma flow and the experimental conditions are described in Chapter III. Experimental results of the interaction between the plasma flow and the magnetic field are given in Chapter IV. A theoretical analysis of the interaction at a large Hall parameter was made using the gasdynamic equations, the generalized Ohm's law and the Maxwell's equations to explain the experimental results. Results are given in Chapter V. The experimental and theoretical results are compared and discussed in Chapter VI.

II. Experimental Apparatus

The experimental apparatus consists of the arc plasma jet, the vacuum system, the magnetic field and the instruments for measurement. The general set-up is shown in Fig. 1.

II-1. *Plasma Generator*

The direct current arc discharge was used as the plasma source. As is shown in Fig. 2, the discharge electrodes are composed of a cathode of tungsten rod and of an anode nozzle made of copper. The throat diameter of the nozzle is 1.2 cm and the exit diameter is 2.0 cm. The distance between the two electrodes are variable from zero up to 1.0 cm. Both electrodes are water-cooled. Two electrodes are insulated from each other by the use of a bakelite block, and the anode nozzle is grounded. At low pressure the cathode spot of an arc discharge tends to spread towards upstream. A quartz tubing was used to constrict the arc current to the tungsten tip. A small tap was drilled through the arc chamber wall to

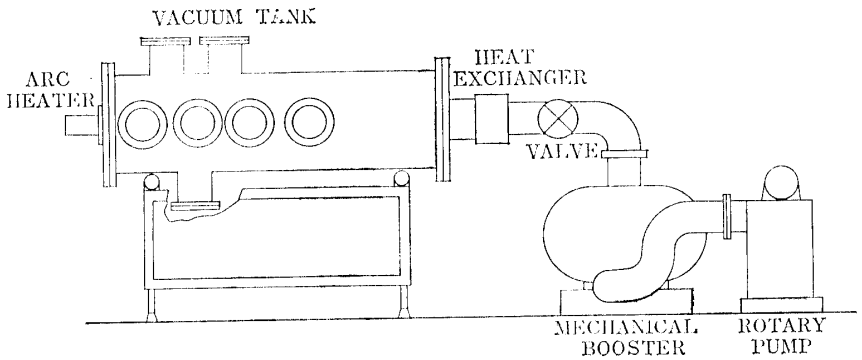

Fig. 1. Experimental facility.

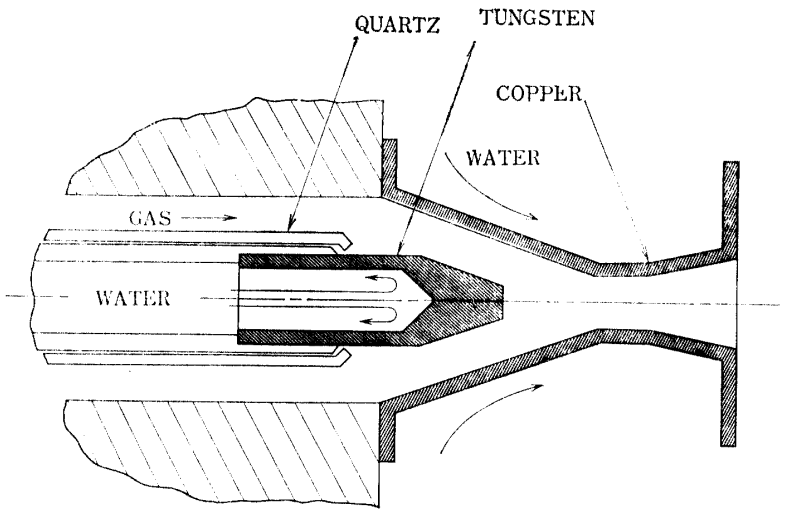

FIG. 2. Electrode configuration.

measure the pressure.

The power supply of the plasma generator is composed of a three-phase full wave rectifier, a saturated reactor controller, and the arc discharge is initiated by applying a radio-frequency voltage. The maximum current of the rectifier is about 800 amperes. The r.m.s. voltage ripple is less than 0.1% of the mean value.

The commercial argon with the purity of 99.999% was used as a working gas. Reasons of the use of argon are that such monoatomic gas is free from dissociation and that the thermodynamic properties and the data of atomic processes are available.

The gas was supplied to the arc chamber in the axial direction through a pressure-regulating valve, a flow meter and a control valve.

The flow duration was more than one minute, and the steady plasma flow was obtained.

II-2. *Vacuum System*

The vacuum tank was made of SUS 27 stainless steel. The diameter and the length are 60 and 200 cm, respectively. The inner surface of the tank was polished to minimize outgassing. On one of the end flange the plasma generator was mounted. On the other end flange an 8 inch pipe was connected, through which the tank was evacuated.

To observe the inside of the tank there are 4 viewing ports with 20 cm diameter glass on each side of the tank. The pressure of the tank was measured by a Pirani gauge mounted on the tank wall. A bakelite flange was mounted on the top, and electric power and signals were transmitted through it. The tank was electrically grounded.

The tank was evacuated by an ULVAC PMB-035 mechanical booster pump and two ULVAC PKS-030 oil rotary pumps. The mehanical booster pump has the pumping speed of 3.5×10^6 liters/hour, and each of the two oil rotary pumps lined parallel has speed of 3000 liters/minute. Pressure of the tank reaches

about 0.005 Torr without supply of the working gas. The tank pressures with 0.06 and 0.15 g/sec of argon flow rate were 0.1 and 0.2 Torr, respectively.

II-3. *Magnetic Field*

The magnetic field was generated by the current through a ring coil. The coil has a 1 cm i.d. and a 21 cm o.d. and is 5 cm thick. The inner diameter of 10 cm has been determined by the photographic observations as the smallest one not to disturb the plasma flow. The metal wall of the coil was coated with alumina cement to prevent the plasma from being in contact with the metal wall. The coil cosists of about 500 turns of copper wire wound on a brass reel. The coil was placed in the tank 10 cm downstream of the exit of the anode nozzle and the electric current to the coil was supplied through the bakelite flange. The calculated magnetic lines of force are shown in Fig. 3, together with the relative positioning of the tank wall and the plasma generator. The coordinate system is taken as shown in Fig. 3, with its origin at the center of the coil.

The axial component of the magnetic field on the center-line is shown in Fig .4. The solid line shows the calculated value under the simplification of replacing the 500 current loops into a single loop of 15.5 cm diameter at the center circle of the coil. The experimental points are obtained from the measurement using a magnetic-flux sensor. The agreement is quite well. The radial component of

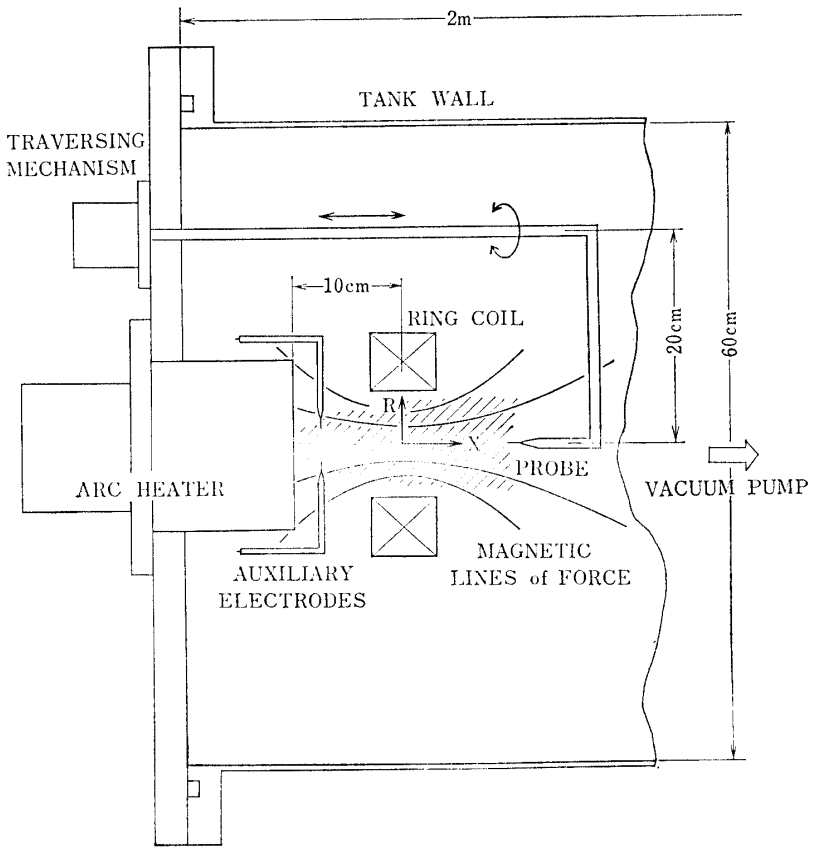

FIG. 3. Layout of experimental setup.

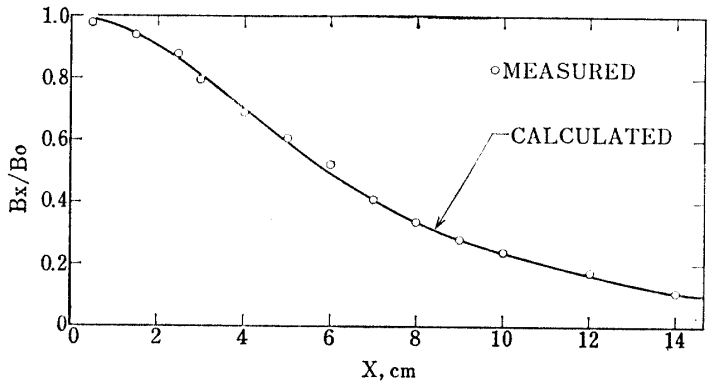

FIG. 4. Axial component of magnetic flux density at $R=0$. Bo is flux density at $X=0$.

the magnetic field was also compared between the measured and calculated values. The agreement is also excellent.

II-4. *Measuring Instruments*

Several kinds of the diagnostic technique were used to obtain the properties of the arc plasma flow in the present experiment. Among them, experimental results with sufficient reliability were obtained by the use of a spectroscope, an electrostatic probe, $U\times B$ velocity meter and an impact pressure probe.

The instrumentations of these measurements are described in the following subsections.

1) Spectroscope

An RM 23 spectroscope with a diffraction grating was used for the spectroscopic measurements of the light emitted from the plasma. The dispersion is 16.5 Å/mm. Spectrographs were taken with Polaroid Type 57 photographic paper. For the measurement of the spectral components the output from the exit slit was detected by a photomultiplier-tube RCA 6199 and indicated on an X-Y recorder. The wavelength was transformed into voltage by connecting the axis of rotation of the diffraction grating to a helical potentiometer. The voltage was fed to the one axis of the X-Y recorder.

The sensitivity and the linearity of the system at the wavelength ranging from 3500 to 5000 Å were determined with the combination of a tungsten lamp at the color temperature 2854°K and the gelatine step down filters.

2) Electrostatic Probe

An electrostatic probe with a cylindrical shape was used. Such a probe is easy to construct, and the surface area is clearly defined. An ideal spherical probe is difficult to fabricate. A plane probe is undesirable since its area, surrounded by the insulator, is uncertain and difficult to be cleaned. In the most of the measurements the probe was placed with its axis parallel to the flow to avaid the effect of the flow. Probes were made of tungsten wires of 0.1 to 1 mm in diameter and of 5 to 10 mm in length. The wires were inserted into a glass

tube and sealed. One of the indispensable treatment in using electrostatic probes is the cleaning of the probe surface. The cleaning was made by flashing the probe surface with 50 Hz ac of 160 V between the probe and the grounded anode of the arc heater in the flow of ionized gas. The cleaning process made the probe measurement reproducible.

The operation of the above apparatus as a well-known Langmuir probe affords the electron temperature and the ion number density. The probe voltage was supplied from the batteries and the 50 Hz commercial line through the isolation transformer. The voltage-current characteristics were displayed on the oscilloscope and photographed. The electron temperature was obtained from the gradient of a semi-logarithmic plot of the voltage-current characteristics. The number density of ions was obtained using the analysis developed by Laframboise [6]. The circuit for the Langmuir probe operation is shown in Fig. 5.a). The maximum current extracted from the plasma flow by the probe was less than 200 mili-amperes, which is far smaller than the current of about 20 amperes equivalent to the total ion flux through a cross section of the jet. The flow field, therefore, is not perturbed by the probe.

The saturation current of ions was measured by fixing the probe bias deeply negative, and was recorded on the X-Y recorder. Under the assumption of the

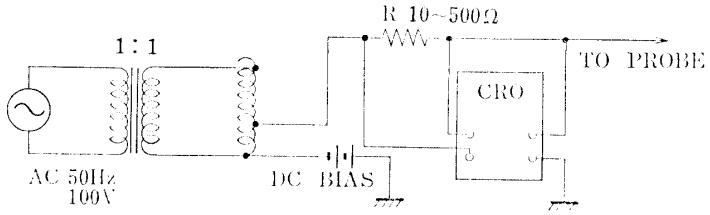

(a) VOLTAGE-CURRENT CHARACTERISTICS

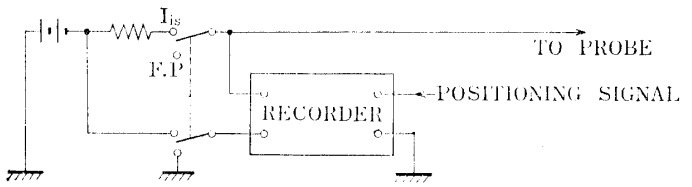

(b) SATURATION ION CURRENT AND FLOATING POTENTIAL

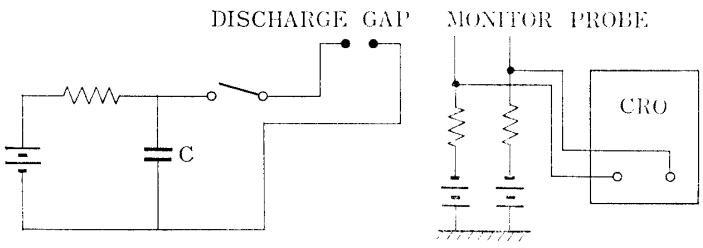

(C) TIME OF FLIGHT VELOMETRY

FIG. 5. Circuitry for electrostatic probe.

constant electron temperature, the saturation ion current can be taken as the indication of the number density of ions. The measurement of the saturation ion current is scarcely affected by the existence of the magnetic field if the Hall parameter of ions is small compared to unity.

The space potential of the plasma can be obtained in principle from the voltage-current characteristics. But in reality, there has been several methods in determining the space potential which often afford different values. In addition, the effect of the magnetic field is quite distinguished near the space potential when the Hall parameter for electron is larger than unity. To avoid these uncertainties, the floating potential, the potential at which no current is collected by the probe, has been used as representing the space potential of the plasma. The difference between the space and floating potentials is a function mainly of the electron temperature and is expressed by the following equation [7]:

$$V_f - V_p \approx -(kT_e/2e) \ln (2m_i/\pi m_e). \qquad (1)$$

Therefore, it is reasonable to regard the floating potential as an indication of the space potential, if the electron temperature is uniform over the region in concern. The experimental results of the distribution of the electron temperature are to be given in Chapter III, and the above condition is concluded to be satisfied well. The floating potential was measured by connecting the probe directly to the X-Y recorder which has the input impedance of more than 100 KΩ. The circuitry is shown in Fig. 5.b).

For the velocity measurements, a set of an auxiliary discharge electrodes and two electrostatic probes was used. The discharge in the upstream region of two probes introduces an additional plasma puff into the original plasma flow. Two probes which were placed with a known distance apart in the streamwise direction were negatively biased to detect time-of-flight of the ion puff. The traces of the two probe currents were displayed on an oscilloscope. The time difference of the traces affords the velocity of the flow. The auxiliary discharge was made by discharging a capacitor of about 40 μF. The voltage and the capacity were varied in several ways to keep the disturbance by the discharge low enough but with measurable intensity. The circuit associating with the time-of-flight method of the velocity measurements is shown in Fig. 5.c).

3) $U \times B$ velocity meter

The $U \times B$ velocity meter is composed of a transverse magnetic field and a double probe. The meter morks by the scheme described in Fig. 6. Suppose a uniform flow begins to pass between two parallel insulting wall from some instance. The ions and electrons are deflected in the opposite Y directions by Lorentz force due to the uniform magnetic field and stay on the surface of the insulator to establish an electic field E_Y. Thereafter the current J_Y is interrupted to flow by E_Y and tends to zero in an equilibrium state. The equibrium value of E_Y is given by Ohm's law equating $J_Y = 0$. The double probe is used to measure E_Y.

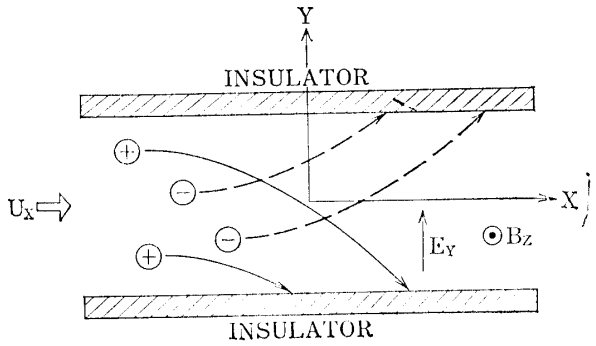

FIG. 6. Scheme of $U \times B$ velocity meter.

When $U \times B$ velocity meter is used, the following conditions must be satisfied:

1. disturbances to the flow by the applied magnetic field should be small.
2. the applied magnetic field should be uniform.
3. the flow velocity should be uniform.
4. the effective impedance of the plasma, which is estimated to be $kT_e/eI_{i,sat}$, should be much smaller than the input impedance of the measuring instruments.
5. Hall effect and ion slip can be ignored.

These conditions are satisfied in the present experiment except the third one. The effect of the nonuniformity of the velocity distribution will be discussed later.

The block diagrain of the measuring circuit is shown in Fig. 7. The magnetic field B is produced by the ac current from 50 Hz commercial line. This enables us to eliminate unwanted dc voltages, such as the surface potential and the sheath drop of the probe. The electric field induced by the alternating magnetic field can be ignored.

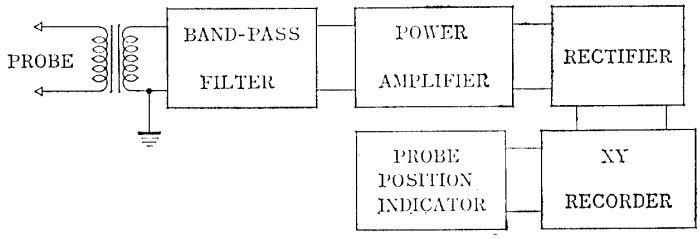

FIG. 7. Block diagram of $U \times B$ velocity meter.

4) Impact-pressure Probe

The impact pressure was measured with a copper tubing with inner and outer diameters of 4 and 6 mm, respectively. It is placed parallel to the flow. The pressure was transformed into voltage by the Pirani gauge and was recorded by an X-Y recorder. The time lag of the indicatoin was minimized by reducing the length of a tubing which is connected to the gauge.

5) Traversing Mechanism

The probes were mounted on the traversing mechanism, and were moved in the plasma. A vacuum-sealed driving shaft is mounted on the end flange 20 cm apart from the center axis and is extending in the tank. A driving motor and a reduction gear system rotate the driving shaft. The angle of rotation was transformed into voltage by a potentiometer and was recorded with an X-Y recorder. The traversing speed was controlled by changing voltage of the driving

motor, and ranged from about 0.5 to 10 cm/sec. The axial positioning was made manually. The error in positioning is estimated to be less than 1 mm in the radial direction and about 2 mm in the axial direction.

III. Experimental Results without Magnetic Field

It is desirable that the plasma flow is uniform in the streamwise direction and have a large Hall parameter for the purpose of the present experiment. The flow field without magnetic field were investigated with the spectroscope, electrostatic probe, impact-pressure probe, the time-of-flight method and the U×B velocity meter. The arc current of 600 amperes was used for most of the experiments. The arc voltage showed little change when the flow-rate of argon and the discharge gap is varied and is about 25 volts.

III-1. *General Features*

The visual observation of the light emitted from the flowing plasma indicates, at large flow-rate of argon, the existence of a shock wave just downstream of the exit of the anode nozlze. In Fig. 8-a) is shown a photograph taken at the flow-rate in of 0.30 g/sec. The increase of the light intensity at X=0 demonstrates the existence of a shock wave. Further downstream the intensity seems to increase again. This is because the flow expands and then forms a weak shock wave

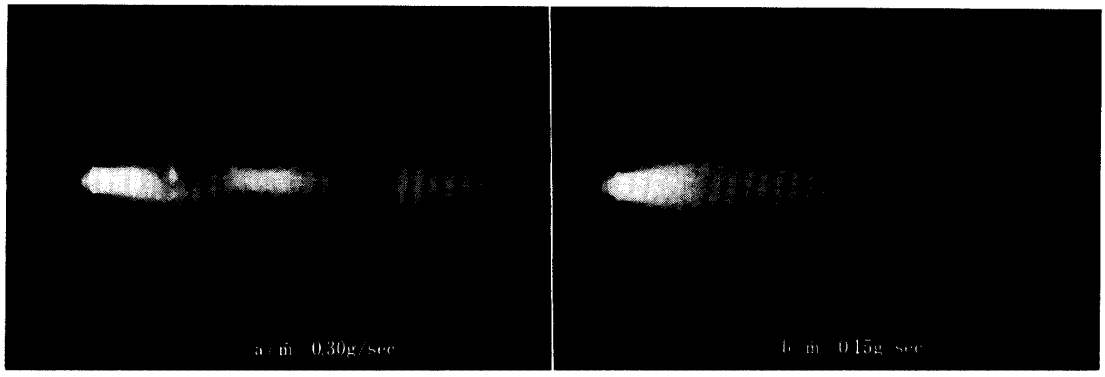

Fig. 9. Plasma flow at various flow rates.

again. At the larger flow-rate the existence of the shock is more distinguished, and its location is shifted a little downstream. The photograph at $\dot{m}$=0.15 g/sec is given in Fig. 8-b), in which the shock pattern becomes more diffuse. At about X=−5 cm, a dark region surrounded by a little more luminous region can vaguely be observed. At $\dot{m}$=0.06 g/sec, the shock pattern can hardly be observed. It is thus suggested that a $\dot{m}$=0.06 g/sec, the flow is so tenuous that the barrel shock is no longer observable.

The pressure of the arc chamber at $\dot{m}$=0.15 g/sec was about 10 Torr and is about 50 times the tank pressure of 0.2 Torr. The anode nozzle has the diameter of 1.2 cm at the throat and 2.0 cm at the exit. The area ratio is 2.8.

The isentropically expanding flow with a specific heat ratio of 5/3 should show the pressure of 0.05 times stagnation pressure at the exit of the nozzle. Thus the flow emanating from the anode nozzle is an under-expanded jet, and the shock is expected to appear downstream.

The saturation ion current from the negatively biased electrostatic probe was measured for the purpose of obtaining the ion density distribution in the flow field. In Fig. 9 is shown the radial distribution of the saturation ion current measured at $\dot{m}$=0.15 g/sec. The distribution at X=5 cm shows peaks at about 1 cm off center. This is an evidence of the existence of a weak shock. Distributions at other positions and those at $\dot{m}$=0.06 g/sec do not show two peaks. The axial distributions of the same quantity on the centerline measured at various flow-rate are given in Fig. 10. At $\dot{m}$=0.30 g/sec, a peak exists at about X=1 cm. This fact is consistent with the luminous region in Fig. 8-a), and the peak is thought to indicate the existence of a shock wave. At $\dot{m}$=0.60 g/sec, the second peak appears at X=12 cm, indicating the existence of another shock wave. On the other hand, a monotonous decrease is shown at $\dot{m}$=0.06 g/sec. The presence of the shock wave in the flow-field is not desirable for the purpose of the present experiment. If a shock wave should appear as a result of the interaction with the magnetic nozzle, it might be a subject of the present investigation. But how the shock is affected by the magnetic nozzle, is not the problem to be studied in the present experiment. Therefore, the experimental condition should be selected so that the properties of the flow are to be as uniform as possible in the axial direction. The flow-rate of working gas is, therefore, decreased as much as possible. Along with the fact that the more tenuous is the plasma the larger

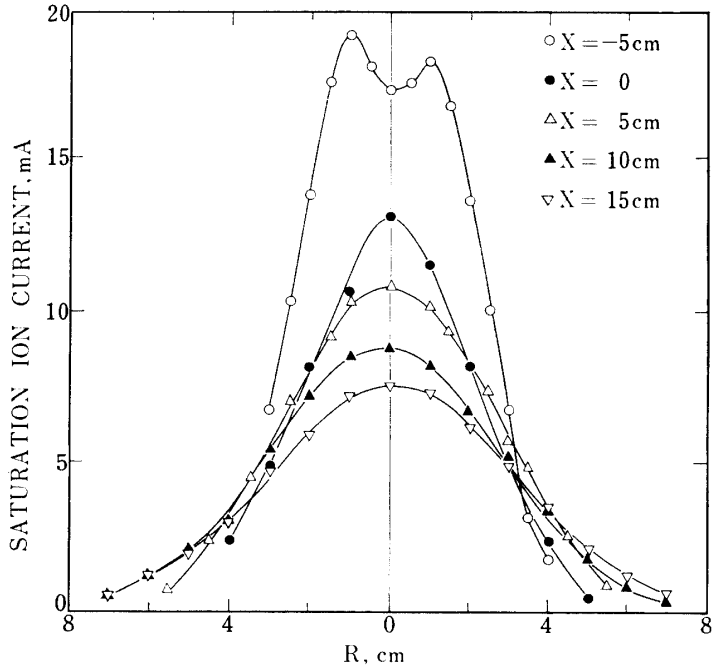

FIG. 9. Radial distribution of saturation ion current. $\dot{m}$=0.15 g/sec and B_0=0.

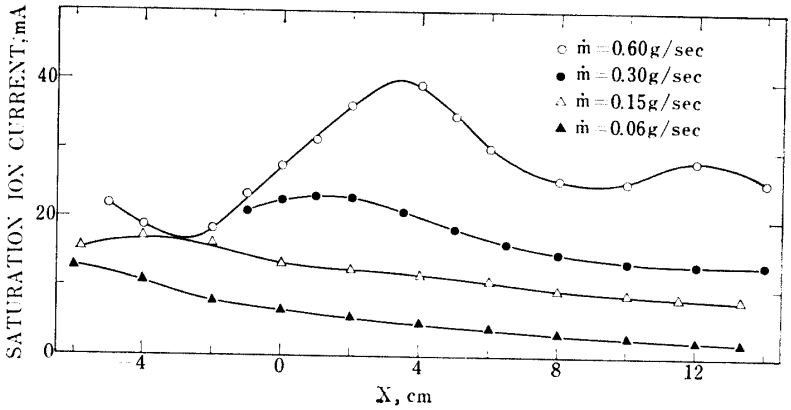

FIG. 10. Axial distribution of saturation ion current for several flow rates, $B_0=0$.

is the Hall parameter, the flow-rate of 0.15 or 0.06 g/sec is expected to be compatible with the requirement of the present experiment. The reasons of the use of the flow-rate of 0.15 g/sec in spite of the existence of the shock wave are as follows: the arc discharge at $\dot{m}=0.15$ g/sec is more stable than at $\dot{m}=0.06$ g/sec; the axial decrease of the saturation ion-current is slower; the experimental values are more reliable partly because of the less fluctuation in the flow field. As to the case of $\dot{m}=0.06$ g/sec, the discussion is to be given in the section III-2 and III-3 in relation to the mean-free-path.

III-2. *Spectroscopic Studies and Electrostatic Probe Measurements*

In order to clarify the composition of the plasma the spectral photographs of the light emitted from the plasma were taken. A typical example near the center-line at X=−10 cm is shown in Fig. 11 taken at the flow-rate of 0.15 g/sec and at 600 amperes arc current. Strong line spectra are mostly of excited argon, ArI and of tungsten, the cathode material. A rough estimation was made of the fraction of tungsten atoms to argon, from the consumption of the cathode and the operation time. It has been confirmed that the number of tungsten atoms in the flow is not more than 0.5% of argon atoms and ions. No lines of copper, the anode material, are found. Lines of H and C were not found either. Therefore, the flow is concluded to be almost free from a contaminating material.

The temperature measurement was made comparing the relative intensity of the lines of ArI. The wavelength range was chosen near 4000 Å where a lot of ArI lines are found and have strong intensity. Reliable transition probabilities are available for these lines [*8*] [*9*].

The intensity of the emission due to the transition from j-state to i-state is expressed in the following form:

$$I_{ji} \propto n_j A_{ji} h\nu_{ji} = \frac{g_j N}{\sum_j g_j} \exp\left(-\frac{E_j}{RT}\right) \cdot A_{ji} h\nu_{ji} \qquad (2)$$

in which g_j is the number of degeneracy, A_{ji} the transition probability, ν_{ji} the

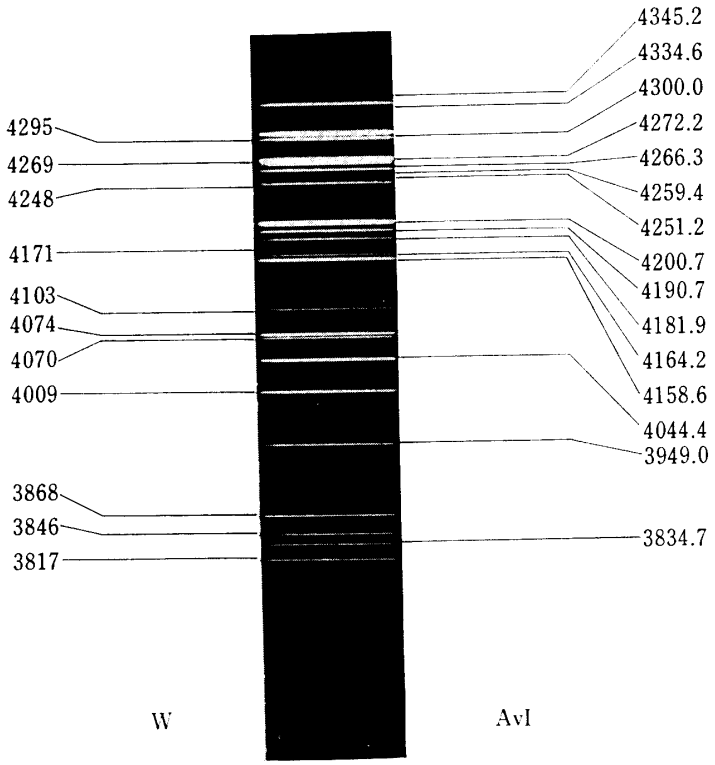

FIG. 11. Spectrograph of radiation emitted from arc jet $X=-10$ cm and $R=0$. $\dot{m}=0.15$ g/sec.

frequency, N the number of particles, and E_j the energy level. Fig. 12 shows a semilogarithmic plot of the relative intensity of the lines against the energy level at X=−6 and 5 cm at $\dot{m}=0.15$ g/sec. Each of the lines was measured at least three times and the results were averaged rejecting the data differing more than 15% from the mean value. Since the reproducibility was good, the above rejections were seldom done. The gradient of the semilogarithmic plot gives the temperature which is also indicated on the figure. The measurements were also performed at the other axial positions to obtain the distribution on the center-line. The resulting temperature distribution is shown in Fig. 13 with open

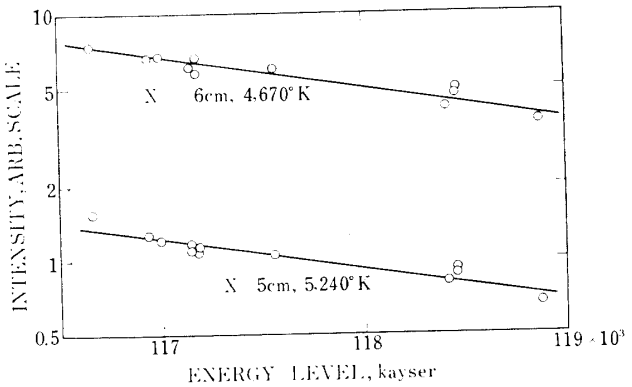

FIG. 12. Relative intensities of ArI lines, $\dot{m}=0.15$ g/sec and $B_0=0$.

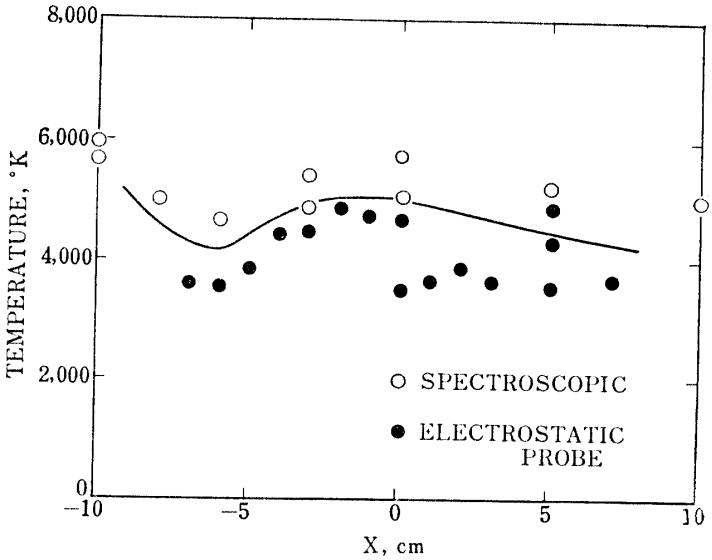

FIG. 13. Temperature distribution on the centerline, $\dot{m}=0.15$ g/sec and $B_0=0$.

circles for the flow-rate of 0.15 g/sec. The temperature is about 5500°K and shows a little variation in the axial direction. This temperature is, according to Adcock, close to that of electrons, to which the higher atomic quantum levels are equilibrating.

The electron temperature measured on the center-line at $\dot{m}=0.15$ g/sec with the electrostatic probe is also shown in Fig. 13. The agreement with the temperature measured spectroscopically is quite well. The axial variation, as a whole, is very small.

The number density of ions is calculated from the saturation ion current and the electron temperature. Values at X=0 are 4.5 and 1.1×10^{13} cm^{-3} at 0.15 and 0.06 g/sec flow-rate, respectively. Under the assumption of the thermal equilibrium at the pressure of 0.2 Torr and temperature of 5000°K, the ionization fraction is calculated to be 0.006%, the number densities of ions and neutral atoms should be 2×10^{10} and $3.3\times^{14}$ cm^{-3}, respectively, according to the Saha-equation. The larger number density of ions obtained experimentally suggests that the plasma is not in thermodynamic equalibrium and it may be in a frozen state. The measured ionization fraction is about 3%.

The mean-free-path of electrons between collisions can be estimated from the measured temperature and number density. The collision with ions is dominant and mean free path are 2.2×10^{-2} and 6.6×10^{-2} cm for $\dot{m}=0.15$ and 0.06 g/sec, respectively. The Hall parameter of an electron at the magnetic field of 1000 gauss is calculated to be 11 and 33 for $\dot{m}=0.15$ and 0.06 g/sec, respectively.

The distribution of the floating potential was measured as an indication of the space potential using an electrostatic probe. As has been noted in II-4.2, the difference between the floating- and space-potentials is proportional to the electron temperature. Since the electron temperature shown in Fig. 13 is almost uniform, the electric field in the flow can be understood by the measurement of the floating-

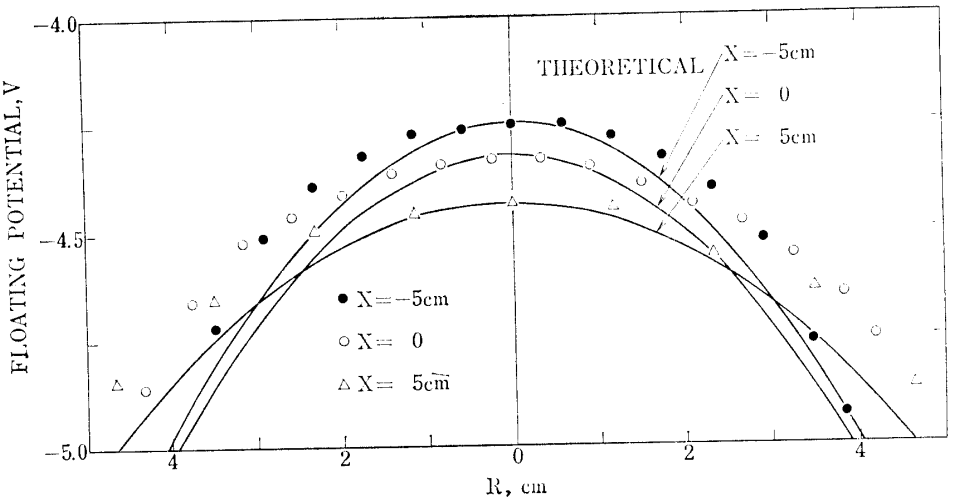

FIG. 14. Radial distribution of measured and calculated flocating potential for several X positions, $\dot{m}$=0.15 g/sec and B_0=0.

potential. In Fig. 14 is shown the radial distribution of the floating-potential at $\dot{m}$=0.15 g/sec. The distributions are almost similar. They have maximum on the centerline and show an outward electric field in the radial direction. The electric field in the flow direction of about 2 V/m is observed on the centerline. The radial electric field becomes weaker further downstream position, but is the order of 10 V/m at about R=4 cm. The distribution at $\dot{m}$=0.06 g/sec show the the same characteristics. It is easily conjectured that these electric fields are caused by the ambipolar diffusion of charged particles from the plasma flow. We made a simple calculation of the diffusion equation. We assume that the loss mechanism of charged particles is the ambipolar diffusion only in the radial direction. The ambipolar diffusion in the axial direction is neglected because the electric field in the axial direction is smaller than the radial field. The ambipolar diffusion coefficients of 1.2×10^4 and 2.1×10^4 cm^2/sec were used for $\dot{m}$=0.15 and 0.06 g/sec,

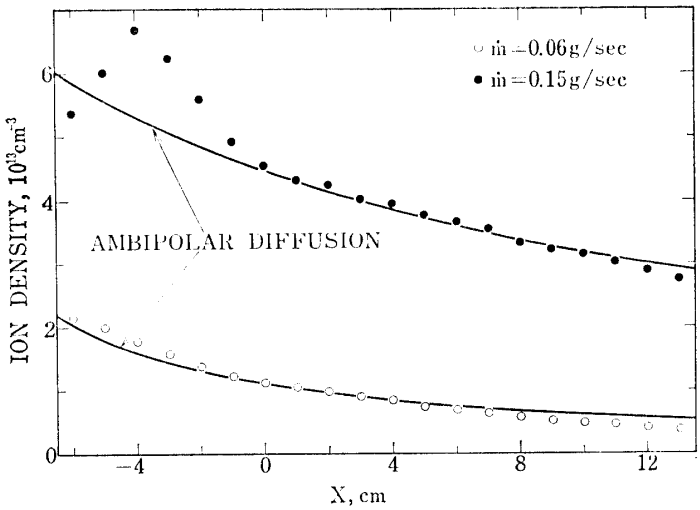

FIG. 15. Axial distribution ion number density at R=0 and B_0=0.

respectively. The ion temperature of 1600°K is used to obtain the diffusion coefficient. The estimation of the ion temperature is to be given in the following subsection. The calculated distributions of the radial electric field and the number density of the charged particles on the centerline are shown in Fig. 14 and 15 respectively together with the experimental values. The agreement is satisfactory.

The decay distance due to the recombination of charged particles is also estimated. A radiative recombination and a three-body recombination are very slow. The characteristic lengths of a recombination of those processes, the length for the number density to become half, are of the order of 10^2 and 10^3 cm, respectively, when U=1.5 km/sec. The dissociative recombination of molecular ion is, on the contrary, very fast. The characteristic length is only 0.1 cm, and is shorter than the experimental results shown in Fig. 13. The fraction of molecular ion is considered to be small from the following estimation. The production rate of molecular argon ions seems not to have been reported as yet. As to He, Johnson et al. [*10*] showed that the production rate is given by $n_i \times 10^4$ /cm^3· sec at the pressure of 27 Torr. Since the production of molecular ions is the result of a tripple collision, the coefficient should vary as the pressure squared. Then at the pressure of 0.2 Torr, the production rate might be given by $n_i \times 0.6$ /cm^3· sec. If we assume that argon ions are removed from the plasma flow of the present experiment at the rate given above, the characteristic length is more than 10^5 cm. It is concluded, therefore, that the flow is frozen as to the recombination and that the particle loss is mainly resulted from the ambipolar diffusion.

III-3. *Velocity and Mach Number Measurement*

The axial velocity of ions in the plasma flow was measured by the time-flight method. One of the typical traces of the transient probe current at $\dot{m}$=0.15 g/sec and at X=15 cm is shown in Fig. 16. The axial distribution of the central velocity is plotted in Fig. 17 for $\dot{m}$=0.15 and 0.06 g/sec. A monotonous decrease downstream is observed.

When the Y distribution of the electric field are measured by the $U \times B$ velocity meter, three peaks are observed. The results in Fig. 18 is obtained by taking

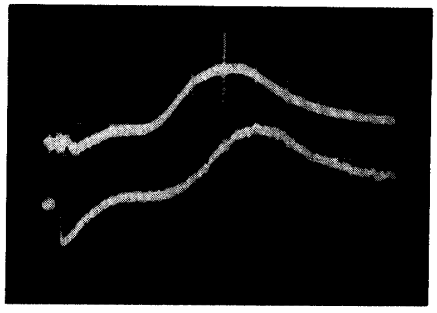

FIG. 16. Typical trace of "time of flight" velocity meter at X=15 cm, $\dot{m}$=0.15 g/sec and B_0=0.

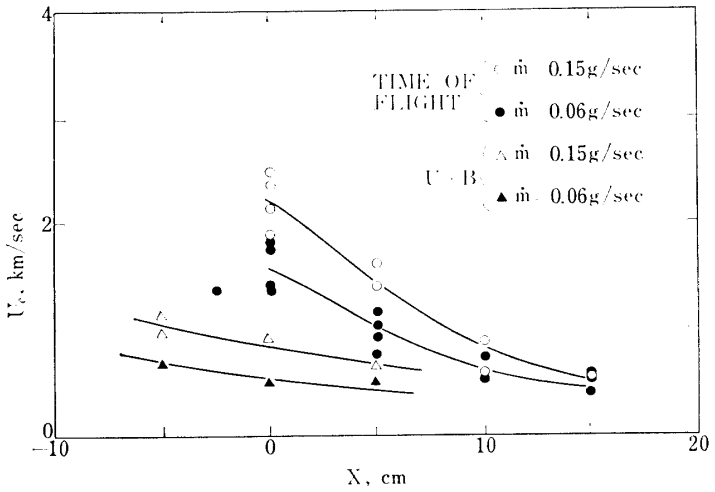

FIG. 17. Axial distribution of velocity at $R=0$ and $B_0=0$.

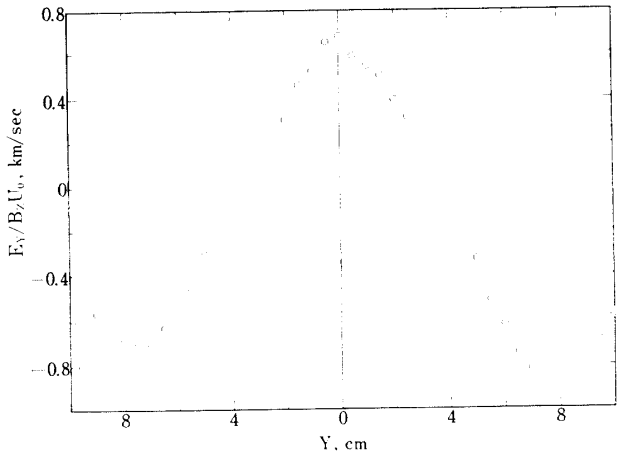

FIG. 18. Electric field distribution of $U\times B$ velocity meter at $X=0$, $\dot{m}=0.15$ g/sec and $B_z=50\,G$.

into account the phase relationship of the 50 Hz component at various Y locations. Negative sign of the electric field is found at large Y location. This comes from the eddy current caused by the nonuniform velocity distribution. Under the assumption of the uniform electrical conductivity the distribution of the electric field is calculated as follows. In the region $|Y|\leq a$

$$E_Y=U_XB_Z-(B_Z/Y^2)\int_0^Y rU_X dr \tag{3}$$

and in the region $|Y|\geq a$

$$E_Y=-(B_Z/Y^2)\int_0^a rU_X dr, \tag{4}$$

where a denotes the radius of jet satisfying $U_X(a)=0$. As a special case a parabolic velocity profile is considered. The electric field E_Y is calculated from

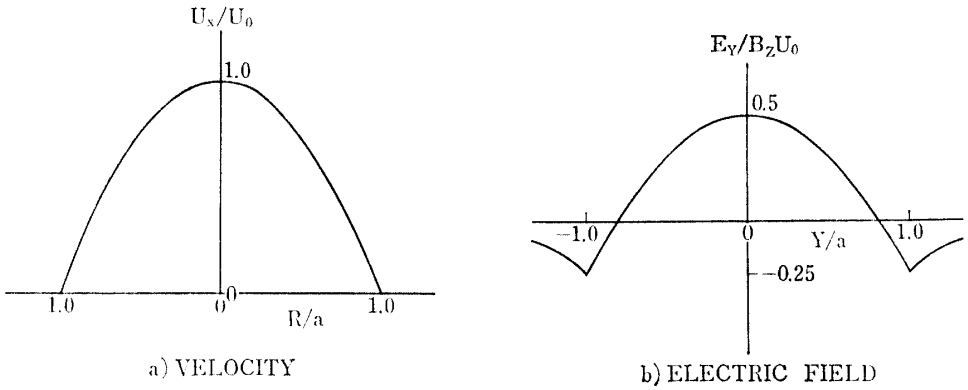

FIG. 19. Calculated distribution of electric field.

the above equations and demonstrated in Fig. 19. When Figs. 18 and 19 are compared, similarity between the distributions in these figures are found.

The results of $U\times B$ method are compared on the center line with those obtained by the time-of-flight method in Fig. 17. Evidently the velocities measured by the $U\times B$ velocity meter are 50% of those measured by the time-of-flight method, which is consistent with the theoretical explanation given above.

Conclutions are derived about the measurements by $U\times B$ velocity meter. The $U\times B$ method is convenient to measure the velocity profile of the plasma flow. Since this method is apt to give smaller velocities, it is desired that an absolute value at one point, for instance on the center line, should be calibrated by an alternative method.

To the impact pressure, heavy particles such as ions and atoms have a dominant contribution. The impact pressure measurement was made to obtain the Mach number. The sound speed or the gas temperature was obtained from the Mach number and the velocity measured by the time-of-flight method. The behaviours of the atoms and ions were assumed to be the same when the magnetic field is absent. Then, we estimated the temperature of ions from the sound speed. In Fig. 20 is shown the axial distribution of the impact pressure normalized by the tank pressure, and of the Mach number at $\dot{m}=0.15$ g/sec. Under the assumption of the existence of a normal shock in front of the probe and the specific heat ratio, γ of 5/3, the Mach number is obtained from the equation;

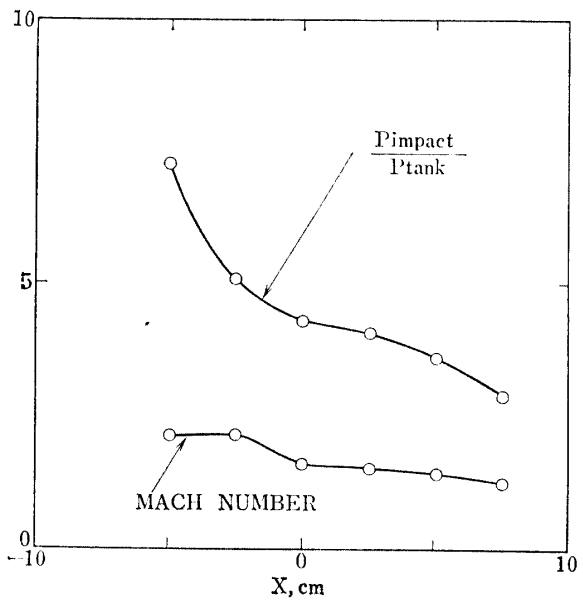

FIG. 20. Axial distribution of impact pressure are Mach number, $\dot{m}=0.15$ g/sec.

$$\frac{P_{\text{impact}}}{P_{\text{tank}}} = \frac{\left(\frac{\gamma+1}{2}M^2\right)^{\gamma/(\gamma-1)}}{\left(\frac{2\gamma}{\gamma+1}M^2-\frac{\gamma-1}{\gamma+1}\right)^{1/(\gamma-1)}}. \tag{5}$$

The Mach number is also decreasing monotomously downstream, but is larger than unity even at X=10 cm. From the velocity and the Mach number the sound speed is obtained, which gives the ion temperature, T_i, of about 1600°K.

The value of the ion temperature gives the estimation of the viscosity μ, the Reynolds number and the mean-free-path of neutral atoms. From the Sutherland formula;

$$\mu = \frac{1.93\times10^{-5}T^{3/2}}{T+142}\ \text{g/cm}\cdot\text{sec}, \tag{6}$$

the Reynolds number per unit length is estimated under the assumption of $T_i=T_a$, to be about 12.4 cm^{-1} for $\dot{m}$=0.15 g/sec. The Reynolds number Re_d based on the outer diameter of the impact pressure probe, 0.6 cm is 7.4. The effect of the small Re_d on the measured impact pressure is discussed by Bailey & Boylan [*11*] and Ashkenas & Sherman [*12*]. According to them, the measured pressure is about 10% higher than the real impact pressure.

The Hall parameters of ions are estimated to be 0.01 and 0.03 from the mean-free-path of 0.003 cm at $\dot{m}$=0.15 g/sec and 0.01 cm at $\dot{m}$=0.06 g/sec, respectively. Electrons are expected to be gyrating around magnetic lines of force, while ions are hardly affected by the magnetic field except indirectly through the motion of electrons. The magnetic Reynolds number, R_m is about 0.1 and therefore deformation of magnetic field by the plasma flow is negligilble.

The behaviour of the Mach disk at low pressure is discussed by Ashkenas & Sherman [*12*]. They reported that when K_m, a Knudsen number based on the diameter of a Mach disk, exceeds 0.1, the Mach disk disappears. In the present experiment the mean-free-path of 1.5 cm for $\dot{m}$=0.15 g/sec. Then K_m is 0.13. When the flow-rate is 0.06 g/sec, mean-free-path is about 0.3 cm and K_m becomes 0.2. Therefore, it is confirmed that the Mach disk is considerably diffused by the viscous effect when the flow-rate is less than 0.15 g/sec.

IV. Experimental Results on the Interaction with a Magnetic Field

In this chapter experimental results on the interaction between the plasma flow and the magnetic nozzle are given. The magnetic field coil is placed 10 cm downstream from the exit of the jet and the flux density at the coil center is 1000 gauss. The position has been selected from the following considerations. It is desired that the magnetic field should be applied on the flow with least axial variation. Also, the arc heater is desired to be unaffected by the magnetic field. As has been shown in the previous seciton, the ion number density and the electron temperature do not change much at X=10 cm. The ion number density

is slowly decreasing when compared with the value at X=−5 cm and the uniformity in X direction is almost satisfactory. The magnetic field at 15 cm apart from the coil center is about 10% of that of the central value. Therefore, the arc discharge and the plasma flow within the anode nozzle might be scarcely affected by the magnetic field.

In order to clarify the detailed mechanism of the interaction, measurements were made on the ion number density, the electron temperature and the potential with electrostatic probes, and the velocity by the time-of-flight method.

IV-1. *General Features of the Interaction*

The visual observation showed two distinct effects due to the application of 1000 gauss magnetic field. First, the flow is strongly pinched. The increase of light intensity is also observed especially in the downstream region from the coil. The feature is clearly shown in Fig. 21, in which Photograph b) has been obtained with the exposure of three-quarters of that of a). As a second effect the luminosity is enhanced near the coil center. In Fig. 22 is given the comparison of the axial distributions of the ion number density on the centerline with and without the magnetic field, at $\dot{m}$=0.15 g/sec. When there is no magnetic field, the saturation ion current reaches the maximum at X=−4 cm. A peak is found

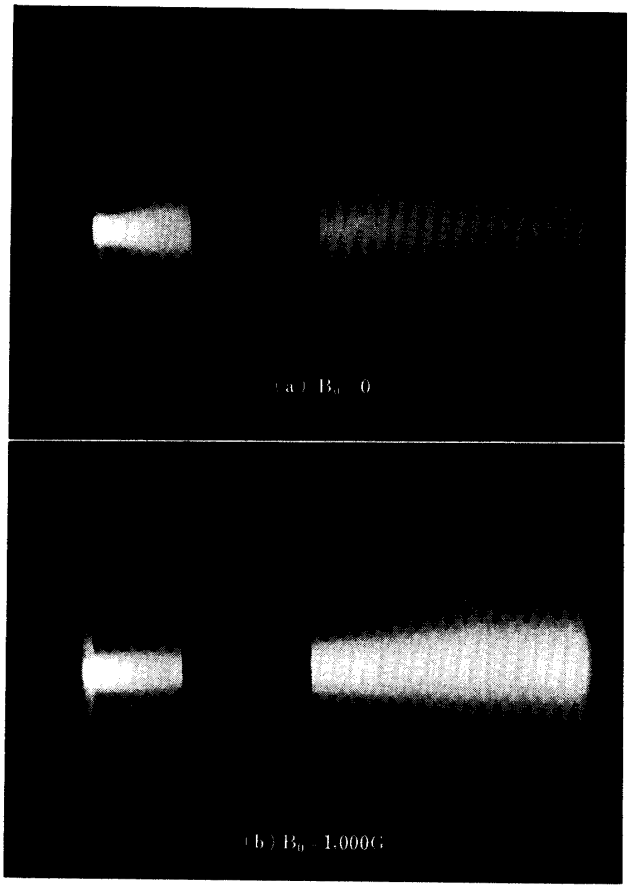

FIG. 21. Photographs of plasma flow with and without magnetic field, $\dot{m}$=0.15 g/sec.

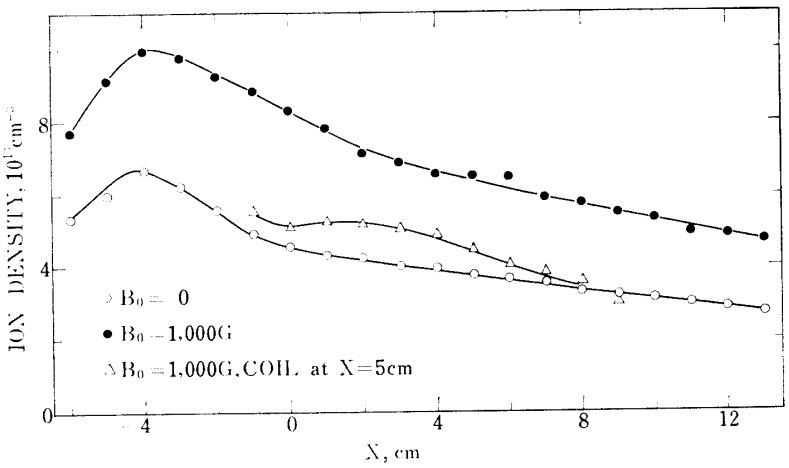

FIG. 22. Axial distribution of ion number density at $R=0$ and $\dot{m}=0.15$ g/sec.

at X=−3 cm when the magnetic field is applied. A similar comparison is given in Fig. 23 at $\dot{m}=0.06$ g/sec. In spite of the monotonous decrease without the magnetic field, a maximum appears at X=−3 cm, the same position as at $\dot{m}=0.15$ g/sec with the magnetic field. In order to confirm that the new peak at X=−3 cm is not resulted from a shock wave, the same measurement was made with the coil at 15 cm downstream from the exit of the arc haeter i.e. 5 cm downstream of the standard position. The resulting distribution of the ion current is plotted in Fig. 22. A peak is found to appear at X=2 cm by the application of the magnetic field. From these experimental results, it is concluded that new peaks which appear in Fig. 22 and 23 are due to the effect of the interaction with the magnetic field. The details of the interaction are to be discussed in Chapter VI.

The pinch effect or the deformation of the plasma boundary due to the magnetic field was examined in detail by measuring the saturation ion current. The radial

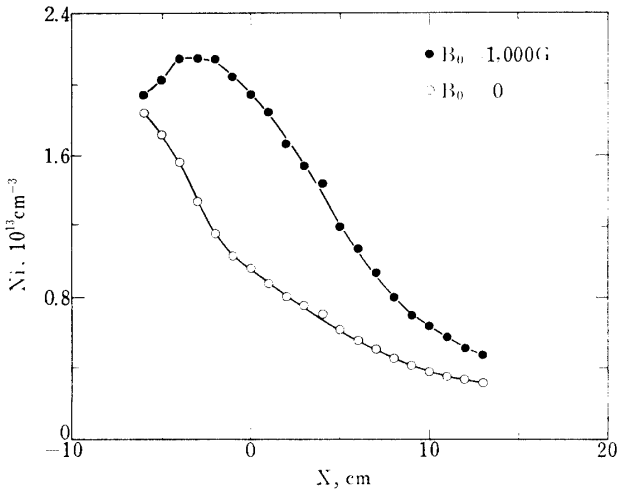

FIG. 23. Axial distribution of ion number density at $R=0$ and $\dot{m}=0.06$ g/sec.

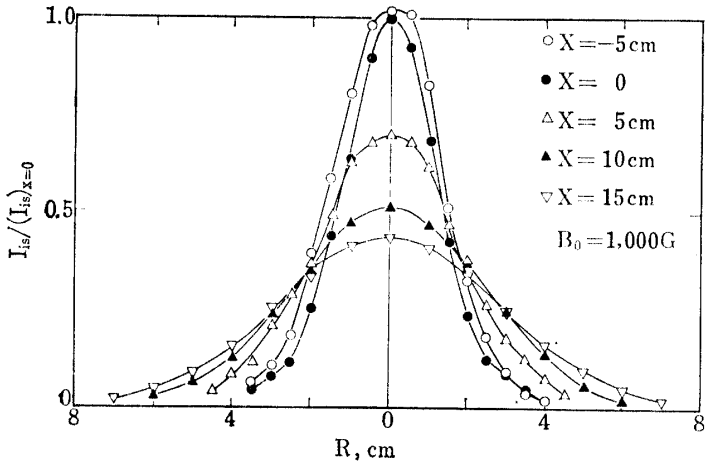

FIG. 24. Radial distribution of saturation ion current, $\dot{m}=0.15$ g/sec and $B_0=1000\,G$.

distributions at various axial positions are shown in Fig. 24 . Clearly shown in the figure are the similar distributions at each axial position and the decrease of the width of the distribution comparing with the distribution without the magnetic field in Fig. 9.

To demonstrate the similarity of the distributions, a nondimensionalization was made with the central value and the half-value radius, the radius at which the saturation ion current becomes a half of the central value. The result is shown in Fig. 25. The solid line shows a Gaussian distribution. The similarity is excellent, and the half value radius is confirmed to be the parameter representing the radial extension of the plasma flow.

In Fig. 26 is shown the axial variation of the half value radius, with and without the magnetic field. The radius reduces by half when the magnetic field is applied. Broken lines show the magnetic lines of force matched with the radii at X=0. The variations of the half value radius agree quite well with the magnetic lines of force when the magnetic field is applied. Charged particles

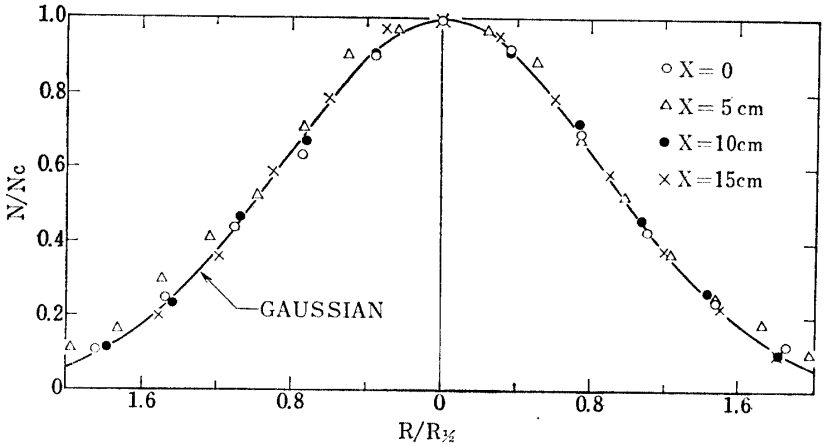

FIG. 25. Radial distribution of ion density for several X positions, $\dot{m}=0.15$ g/sec and $B_0=1000\,G$.

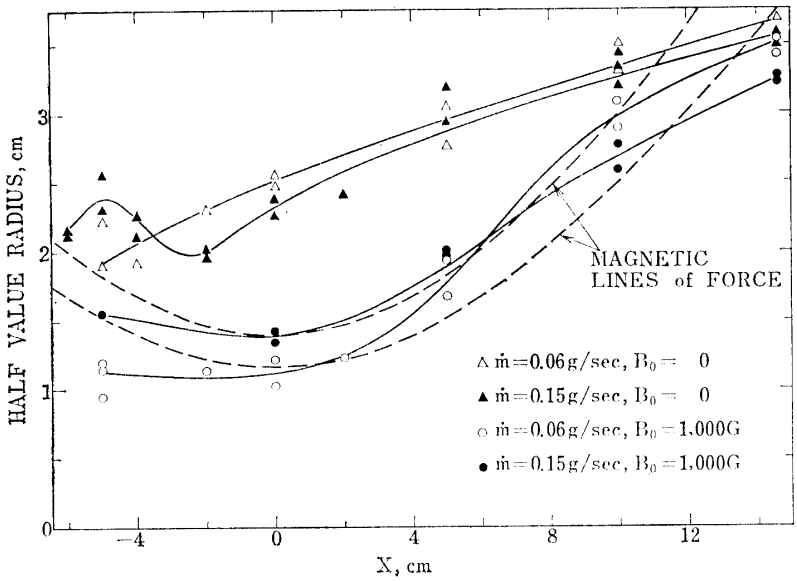

FIG. 26. Axial variation on half value radius with and without magnetic field.

are concluded to flow along the magnetic lines of force. At X=10 cm the magnetic flux density is 230 gauss on the centerline. The half value radius deviates from the magnetic lines of force in the region X>10 cm.

Electron temperature is measured by the electrostatic probe. Only high energy electrons are considered in order to avoid the influence of the magnetic field. The distributions on the center axis at $\dot{m}$=0.15 g/sec is shown in Fig. 27. The distribution without magnetic field is also shown in the same figure. Electron temperature increases about 3000°K at X=0 by the application of the magnetic field. In X>0 the temperature decreases rapidly to the value without magnetic field.

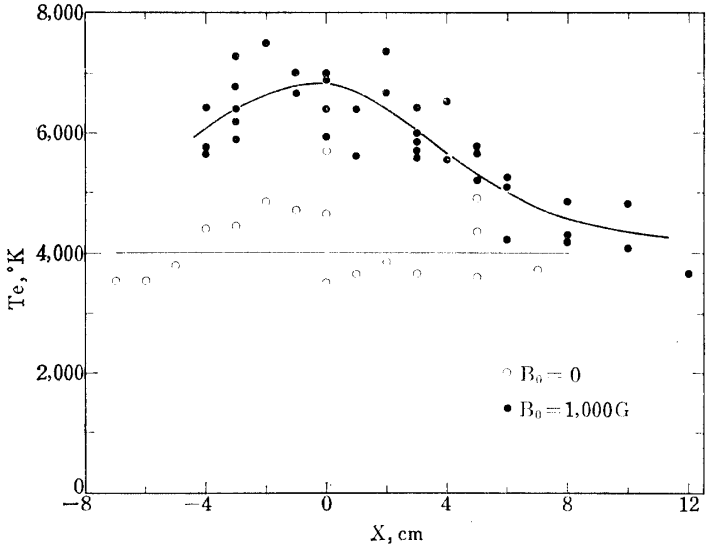

FIG. 27. Electron temperature distribution with and without magnetic field, $\dot{m}$=0.15 g/sec.

The electrons under these conditions, gyrate several times around the magnetic lines of force between successive collisions, and the motion of the guiding center of the electron gyration is along the magnetic line of force. The ions, on the other hand, hardly gyrate between collisions. Then the motion of ions must be governed by the motion of electrons, namely, by the electric field generated as a result of the weak charge separation, and the ions also tend to flow along the magnetic lines of force as is shown in Fig. 23. From the electron temperature and the Poisson's equation, the electric field is estimated to be of the order of 0.1 volt/cm and the difference between the number density of ions and electrons, $(n_i-n_e)/n_i$ to be about 4×10^{-10}. Thus the charge separation is very weak and the quasi-neutrality, $n_i\approx n_e$ holds.

IV-2. *Electric Potential*

As a result of the interaction with the magnetic field, the path of electrons converges towards the centerline in the upstream region of the coil and diverges in the downstream region. Ions, on the other hand, tend to remain on their original paths, namely tend to move nearly parallel to the centerline. Therefore, there results the charge separation and the plasma potential on the centerline is expected to be negative upstream and positive downstream of the coil with respect

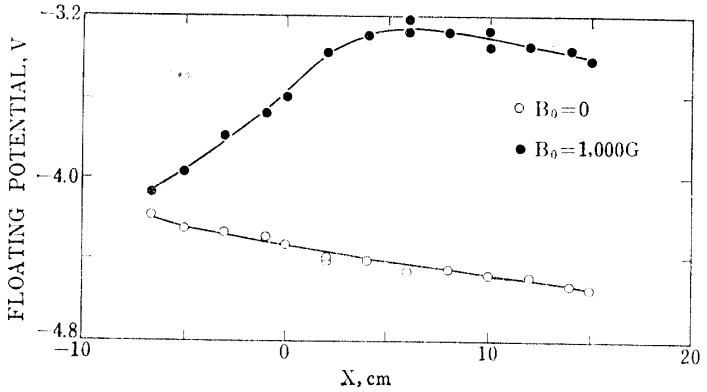

FIG. 28. Axial distribution of floating potential at $R=0$ and $\dot{m}=0.15$ g/sec.

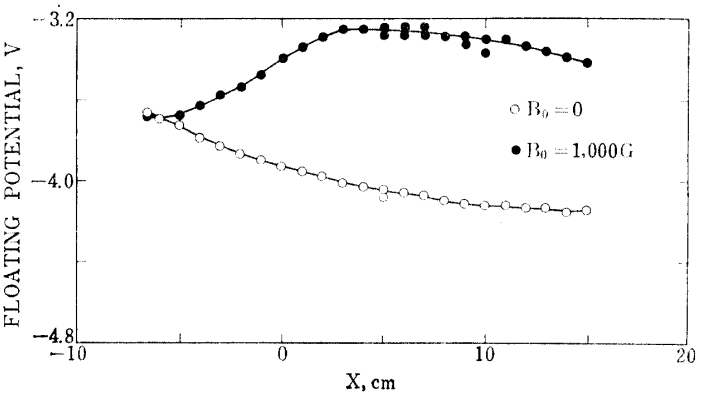

FIG. 29. Axial distribution of floating potential at $R=0$ and $\dot{m}=0.06$ g/sec.

to the potential at the center of the coil. In the absence of a Hall effect no electric field results in the meridian plane. The axial electric field, therefore, is a measure of the Hall effect. The floating potential of the electrostatic probe was used to measure the induced electric field. Axial distributions at $\dot{m}=0.15$ and 0.06 g/sec are shown in Figs. 28 and 29 with and without the magnetic field. When there is the magnetic field, the potential increase rapidly downstream around X=0, the position of the center of the magnetic field. Peaks of the potential are observed at about X=5 cm. In the far upstream region, the potential obtained with the magnetic field approaches to that obtained without the magnetic field.

The radial distribution of the floating potential at $\dot{m}=0.15$ g/sec is shown in Fig. 30. Distributions without magnetic field show the electric field which is induced by the ambipolar diffusion. The distributions with the magnetic field show quite different features. A minimum of the potential at the center is shown in the distribution at X=−5 cm, the upstream region of the coil. At X=7.5 cm, the downstream region, the potential reaches maximum at the center. At further downstream region, the distribution becomes flat near the central region. The distributions near the coil are mostly explained with the motion of electrons along the magnetic lines of force and the charge separation. The ambipolar diffusion is prevented in this region because of the existence of the strong magnetic field. In the region X>10 cm the magnetic field is not strong enough to confine electrons along lines of force. The electric field due to ambipolar diffusion appears again as in the flow field without the magnetic field.

The potential distributitons with the magnetic field are to be compared in Chapter VI with results of the theoretical calculations in Chapter V.

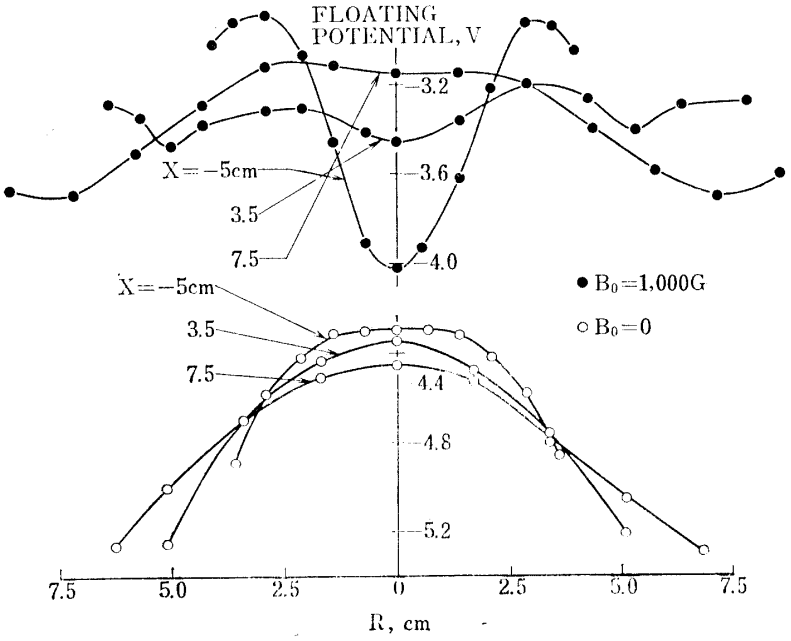

FIG. 30. Radial distribution of floating potential, $\dot{m}=0.15$ g/sec.

IV-3. *Velocity Distribution*

A supersonic flow through a solid nozzle is, as is well known, decelerated in a converging region and then accelerated in a diverging region. The Mach number of the plasma flow of the present experiment has been estimated in Chapter III to be about 2. The velocity distribution in the present experiment is expected to behave like a flow throuh a solid nozzle. Two kinds of measurement were made in order to determine the velocity distribution of the flow through the magnetic nozzle. The measurement by the time-of-flight method affords the velocity of ions and was made mainly on the centerline. By the measurement using an impact-pressure probe the velocity mainly of the neutral atoms is determined.

In Fig. 31 is shown result of the time-of-flight measurement along the centerline, with and without the magnetic field, at the flow-rate of 0.15 g/sec. The ions are shown to be strongly decelerated in the upstream of the coil, reach a minimum velocity at X=0 and then be accelerated downstream. The maximum

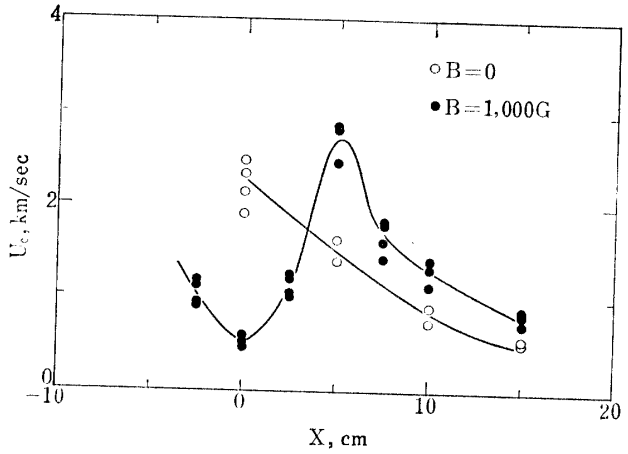

FIG. 31. Distribution of axial velocity with and without magnetic field at $R=0$ and $\dot{m}=0.15$ g/sec.

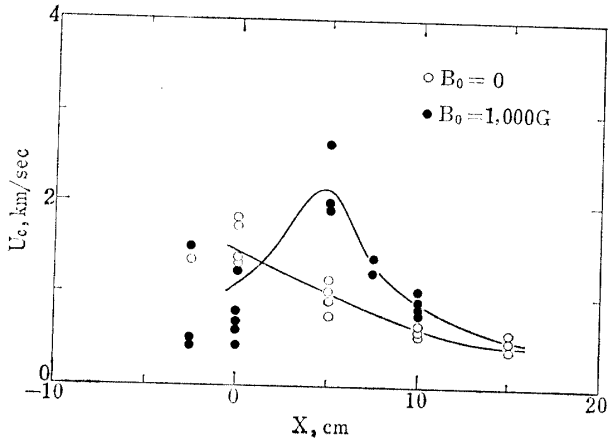

FIG. 32. Distribution of axial velocity with and without magnetic field at $R=0$ and $\dot{m}=0.06$ g/sec.

of 2.5 km/sec is reached at X=5 cm. Further downstream the velocity decreases monotonously. Almost the same features are shown for $\dot{m}$=0.06 g/sec in Fig. 32.

The velocity at X=5 cm and R=2 cm which is the half value radius of the saturation ion current, was measured at $\dot{m}$=0.15 g/sec. The value was about 60% of the central value. The velocity distribution in the radial direction is, therefore, approximately the same as the distribution of the charged particles.

In Fig. 33 are shown axial distributions of the impact pressure and the Mach number on the centerline with the magnetic field at $\dot{m}$=0.15 g/sec. The Mach number is obtained from the normal shock relation. In contrast to the results of the time-of-flight measurement, no drastic change is found at X=5 cm and the monotonous decrease to the downstream is observed. From these behaviours

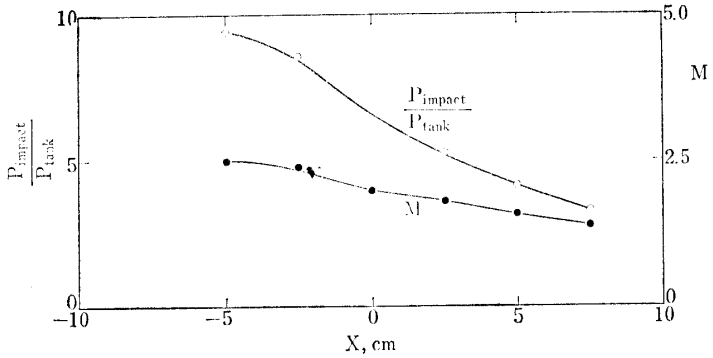

FIG. 33. Distributions of impact pressure and Mach number at R=0 and $\dot{m}$=0.15 g/sec.

of the ion velocity and the impact pressure, the neutral atoms might have a different velocity from that of ions. The existence of the difference between the motion of neutral atoms and ions is confirmed by the non-equipartition of the axial kinetic energy between ions and neutral atoms. If the neutral particles have the same velocity as that of ions, a sound speed is calculated from the velocity and a Mach number to be 1.7 km/sec at X=5 cm. The sound speed of 1.7 km/sec is attained when the argon atoms are heated to 8500°K. This

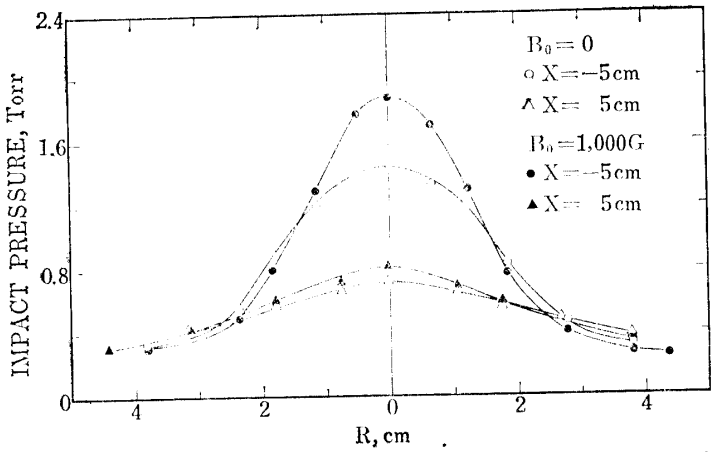

FIG. 34. Radial distribution of impact pressure with and without magnetic field, $\dot{m}$=0.15 g/sec.

temperature is quite unrealistic in view of the 1600°K mentioned previously. Then neutral atoms which have the dominant contribution to an impact pressure, are concluded to behave in a different way from ions. In Fig. 34 is shown the radial distribution of the impact pressure at $\dot{m}=0.15$ g/sec with and without the magnetic field. The increase of the pressure on the centerline by the application of the magnetic field is quite small. This is reasonable because the neutral atoms remain unaffected by the magnetic field.

As a result of the above experiments, the magnetic nozzle has been shown to have the effect selectively on the electron-ion gas as a solid nozzle has on the supersonic flow. A detailed discussion will be given in Chapter VI.

V. Theoretical Analysis

V-1. *Governing Equations*

The gasdynamic equations and the generalized Ohm's law were used to analyse the interaction between the magnetic nozzle and the plasma flow.

The gasdynamic equations in the non-dimensional forms are the continuity and momentum equations [3]

$$\nabla\cdot(\rho V)=0, \tag{7}$$

$$\rho(V\cdot\nabla)V=-\frac{1}{\gamma M_\infty^2}\nabla p+\varepsilon J\times B, \tag{8}$$

in which ρ is the mass density, V the flow velocity, p the pressure, γ the ratio of specific heats, J the current density and B the magnetic field intensity. Throughout the analysis MKS unit are used. The nondimensionalization has been made with $V_\infty, \rho_\infty, p_\infty, B_0$, and L, the radius of the center circle of the coil. Subscript ∞ denotes the quantity at the far upstream region and B_0 is the intensity of the applied magnetic field at $X=0$. The magnetic Reynolds number, R_m is defined as $\sigma\mu V_\infty L$, where σ is the electric conductivity and μ, the magnetic permeability. The interaction parameter, ε is defined as $R_m B_0^2/\mu\rho V_\infty^2$ and indicates the effect of the magnetic field.

The electromagnetic field is expressed under the assumptions of a quasi-neutrality and of a steady state using the Maxwell's equations and the generalized Ohm's law including the Hall effect:

$$\nabla\times E=0, \tag{9}$$

$$\nabla\cdot B=0, \tag{10}$$

$$\nabla\times B=R_m J \quad \text{or} \quad \nabla\cdot J=0 \tag{11}$$

and

$$J=\sigma\left\{E+V\times B+\frac{\alpha}{\rho}\left(\frac{1}{\varepsilon\gamma M_\infty^2}\nabla p_e-J\times B\right)\right\}, \tag{12}$$

where $\boldsymbol{E}$ is the electric field and α the electron Hall parameter, $\omega_e\tau_e$. When the neutral atoms behave in a different way from ions, a term expressing the ion slip must be added in the right side of Eq. (12). In the present analysis the ion slip is neglected.

Under the assumption of the small R_m and ε, the following expansions ate made:

$$\boldsymbol{V}=\boldsymbol{U}_0+\varepsilon\boldsymbol{V}_\varepsilon+R_m\boldsymbol{V}_m+\cdots, \tag{13.1}$$

$$\rho=1+\varepsilon M_\infty^2\rho_\varepsilon+R_m\rho_m+\cdots, \tag{13.2}$$

$$p=1+\varepsilon\gamma M_\infty^2 p_\varepsilon+R_m p_m+\cdots, \tag{13.3}$$

$$p_e=p_{e\infty}+\varepsilon\gamma M_\infty^2 p_{e\varepsilon}+R_m p_{em}+\cdots, \tag{13.4}$$

$$\boldsymbol{B}=\boldsymbol{B}_0+\varepsilon\boldsymbol{B}_\varepsilon+R_m\boldsymbol{B}_m+\cdots, \tag{13.5}$$

$$\boldsymbol{E}=\boldsymbol{E}_0+\varepsilon\boldsymbol{E}_\varepsilon+R_m\boldsymbol{B}_m+\cdots, \tag{13.6}$$

$$\sigma=1+\varepsilon\sigma_\varepsilon+R_m\sigma_m+\cdots. \tag{13.7}$$

Eqs. (7) through (12) can be expanded with the above expressions. Equating the terms with the same powers, following first-order equations in ε for the flow field and the zero-order equations in R_m for the electric and magnetic field are obtained:

$$M_0^2\boldsymbol{U}_0\cdot\nabla\rho_\varepsilon+\nabla\cdot\boldsymbol{V}_\varepsilon=0, \tag{14}$$

$$(\boldsymbol{U}_0\cdot\nabla)\boldsymbol{V}_\varepsilon=-\nabla p_\varepsilon+\boldsymbol{J}_0\times\boldsymbol{B}_0, \tag{15}$$

$$\nabla\cdot\boldsymbol{B}_0=0, \tag{16}$$

$$\nabla\cdot\boldsymbol{E}_0=0 \quad \text{or} \quad \boldsymbol{E}_0=-\nabla\phi, \tag{17}$$

$$\nabla\times\boldsymbol{B}_0= \quad \text{or} \quad \nabla\cdot\boldsymbol{J}_0=0, \tag{18}$$

and

$$\boldsymbol{J}_0=\boldsymbol{E}_0+\boldsymbol{U}_0\times\boldsymbol{B}_0+\alpha\nabla p_{e\varepsilon}-\alpha\boldsymbol{J}_0\times\boldsymbol{B}_0 \tag{19}$$

Put $\Phi=\phi-\alpha p_{e\varepsilon}$, then equation (19) becomes

$$\boldsymbol{J}_0=-\nabla\Phi+(\boldsymbol{U}_0-\alpha\boldsymbol{J}_0)\times\boldsymbol{B}_0. \tag{20}$$

In the above expressions, $\boldsymbol{B}_0$ is the applied magnetic field, and $\boldsymbol{E}_0$ is the electric field which is induced by the interaction. The contribution of electron pressure to Φ can be ignored when the plasma is weakly ionized.

Eqs. (12) and (20) can be solved independently of Eqs. (14) and (15) for the unknown J_0 and Φ for the given initial velocity and external magnetic field. The solution is shown in the next section.

V-2. *Solution in the Axi-Symmetric Case*

The cylindrical co-ordinate system (x, r, θ) is adopted, and the differentiation with respect to θ is zero. The center of the current loop is taken as the origin of the system. Subscript 0 is omitted in the following expressions.

The stream function of the electric current ϕ, defined as:

$$\begin{aligned} J_x &= \frac{1}{r}\frac{\partial \phi}{\partial r}, \\ J_r &= -\frac{1}{r}\frac{\partial \phi}{\partial x} \end{aligned} \tag{21}$$

is introduced. Elimination of Φ and J_θ from Eq. (20) gives the following differential equation for ϕ:

$$\begin{aligned} &\left[\left(\frac{\partial^2}{\partial x^2}+\frac{\partial^2}{\partial r^2}-\frac{1}{r}\frac{\partial}{\partial r}\right)\right. \\ &\quad \left.+\alpha^2\left\{\left(B_x\frac{\partial}{\partial x}+B_r\frac{\partial}{\partial r}\right)-\frac{2B_r}{r}\left(B_x\frac{\partial}{\partial x}+B_r\frac{\partial}{\partial r}\right)\right\}\right]\phi \\ &= r\alpha\left(B_x\frac{\partial}{\partial x}+B_r\frac{\partial}{\partial r}-\frac{B_r}{r}\right)UB_r, \end{aligned} \tag{22}$$

where U is assumed to have only an x component U. The boundary conditions are that $\phi=0$ at $x\to\pm\infty$ and at the jet boundary.

The magnetic field generated by a current loop is expanded near the axis of symmetry in the following form:

$$\begin{aligned} B_x &= F(x)-\frac{1}{4}r^2\frac{d^2F}{dx^2}+\frac{r^4}{64}\frac{d^4F}{dx^4}-\cdots, \\ B_r &= -\frac{r}{2}\frac{dF}{dx}+\frac{r^3}{16}\frac{d^3F}{dx^3}-\frac{r^5}{384}\frac{d^5F}{dx^5}+\cdots, \end{aligned} \tag{23}$$

where

$$F=1/(1+x^2)^{3/2}.$$

The independent variables x and r are then transformed to η and ξ. The magnetic lines of forced by $\eta=$constant, and ξ is the orthonormal co-ordinate. The difinitions of ξ and η are

$$\frac{\partial \xi}{\partial x}=B_x, \qquad \frac{\partial \xi}{\partial r}=B_r, \tag{24.1}$$

$$\frac{1}{r}\frac{\partial \eta}{\partial \gamma}=B_x, \qquad -\frac{1}{r}\frac{\partial \eta}{\partial x}=B_r. \tag{24.2}$$

Eq. (22) is then transformed into a simpler form:

$$\left[B^2(1+\alpha^2B^2)\frac{\partial^2}{\partial\xi^2}+\left\{\alpha^2B^2\frac{\partial B^2}{\partial\xi}-(1+\alpha^2B^2)\frac{2B_r}{r}\right\}\frac{\partial}{\partial\xi}+B^2r^2\frac{\partial^2}{\partial\eta^2}\right]\psi$$
$$=\alpha r\left(B^2\frac{\partial}{\partial\xi}-\frac{B_r}{r}\right)UB_r. \tag{25}$$

The boundary conditions are:

$$\psi=0 \qquad \text{at } \xi=\pm1 \quad \text{and} \quad \eta=\eta_0 \tag{26}$$

where η_0 denotes the boundary of the jet.

Eq. (25) is then expanded in the Fourier series. The magnetic field is approximated in the following form:

$$B_x=(1+\cos\pi\xi)/2, \tag{27.1}$$

$$B_r/r=\pi(1+\cos\pi\xi)\sin\pi\xi/8, \tag{27.2}$$

and ξ and η are from Eq. (24)

$$\xi=\frac{2}{\pi}\tan^{-1}\frac{\pi x}{2}, \tag{28.1}$$

$$\eta=\frac{2r^2}{4+\pi^2x^2}. \tag{28.2}$$

The magnetic field approximated by Eq. (27) is compared in Fig. 35 with Eq. (23). The current stream function ψ is expanded, considering the boundary condition at $\xi=\pm1$, into the following form:

$$\psi(\xi,\eta)=\sum_{m=1}^{\infty}A_m(\eta)\cos\frac{2m-1}{2}\pi\xi. \tag{29}$$

If U is a function of only η, Eq. (25) is rewritten in the form of an ordinary differential equation:

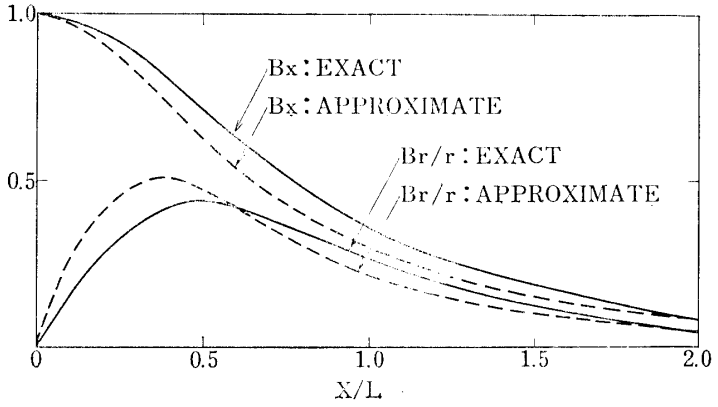

FIG. 35. Magnetic field distribution at $R=0$.

$$\sum_{m=1}^{\infty}\left[(1+\cos\pi\xi)^2\left\{1+\frac{\alpha^2}{4}(1+\cos\pi\xi)^2\right\}\left(\frac{2m-1}{2}\right)^2 A_m(\eta)\cos\frac{2m-1}{2}\pi\xi\right.$$
$$+\left\{1+\frac{3}{4}\alpha^2(1+\cos\pi\xi)^2\right\}\frac{2m-1}{2}A_m(\eta)\sin\pi\xi\cdot\sin\frac{2m-1}{2}\pi\xi \qquad (30)$$
$$\left.+\frac{4\eta}{\pi^2}A_m''(\eta)\cos\frac{2m-1}{2}\pi\xi\right]=\frac{1}{2}U\alpha\eta(\cos\pi\xi+\cos 2\pi\xi),$$

where the prime denotes the differentiation with respect to η. The right side of Eq. (30) is expanded as follows:

$$-\frac{24}{\pi}U\alpha\mu\sum_{m=1}^{\infty}\frac{(-1)^m}{(2m+3)(2m+1)(2m-3)(2m-5)}\cos\frac{2m-1}{2}\pi\xi.$$

The resulting equations for the coefficient of $\cos\pi\xi/2, \cos 3\pi\xi/2$, $\cos 5\pi\xi/2$ and $\cos(2m-1)\pi\xi/2$ $(m\geq 4)$, are:

$$\frac{4\eta}{\pi^2}A_1''-\frac{1}{8}\left(1+\frac{5}{16}\alpha^2\right)A_1-\frac{3}{8}\left(1+\frac{9}{16}\alpha^2\right)A_2$$
$$-\frac{25}{128}\alpha^2A_3-\frac{7}{128}\alpha^2A_4=\frac{8}{15\pi}U\alpha\eta, \qquad (31.1)$$

$$\frac{4}{3}\frac{\eta}{\pi^2}A_2''-\frac{1}{8}\left(1+\frac{9}{16}\alpha^2\right)A_1-\frac{3}{4}\left(1+\frac{19}{32}\alpha^2\right)A_2-\frac{5}{8}\left(1+\frac{5}{16}\alpha^2\right)A_3$$
$$-\frac{21}{64}\alpha^2A_4-\frac{9}{128}\alpha^2A_5=\frac{24}{35\pi}U\alpha\eta, \qquad (31.2)$$

$$\frac{4\eta}{5\pi^2}A_3''-\frac{5}{128}\alpha^2A_1-\frac{3}{8}\left(1+\frac{15}{16}\alpha^2\right)A_2-\frac{5}{4}\left(1+\frac{5}{8}\alpha^2\right)A_3$$
$$-\frac{7}{8}\left(1+\frac{15}{16}\alpha^2\right)A_4-\frac{27}{64}\alpha^2A_5-\frac{11}{128}\alpha^2A_6=\frac{8}{63\pi}U\alpha\eta \qquad (31.3)$$

and for $m\geq 4$:

$$\frac{4\eta}{(2m-1)\pi^2}A_m''-\frac{2m-7}{128\alpha^2}A_{m-3}-\frac{3(2m-5)}{64}\alpha^2A_{m-2}$$
$$-\frac{2m-3}{8}\left(1+\frac{15}{16}\alpha^2\right)A_{m-1}-\frac{2m-1}{4}\left(1+\frac{5}{8}\alpha^2\right)A_m$$
$$-\frac{2m+1}{8}\left(1+\frac{15}{16}\alpha^2\right)A_{m+1}-\frac{3(2m+3)}{16}\alpha^2A_{m+2} \qquad (31.4)$$
$$-\frac{2m+5}{128}\alpha^2A_{m+3}$$
$$=-\frac{24}{\pi}U\alpha\eta\frac{(-1)^m}{(2m+3)(2m+1)(2m-3)(2m-5)}.$$

Then, A_m and U are expanded using the Bessel function of the first order J_1, into the forms:

$$A_m=\sum_{n=1}^{\infty}\frac{4a_{mn}}{\alpha(2m-1)}\sqrt{\frac{\eta}{\eta_0}}J_1\left(\lambda_n\sqrt{\frac{\eta}{\eta_0}}\right),$$
$$U=\sum_{n=1}^{\infty}b_n\sqrt{\frac{\eta_0}{\eta}}J_1\left(\lambda_n\sqrt{\frac{\eta}{\eta_0}}\right)\Big/\sum_{n=1}^{\infty}\frac{\lambda_n}{2}b_n, \tag{32}$$

where λ_n is the n-th root of the equation $J_1(\lambda_n)=0$. The equation (31.4) can be rewritten by means of the orthogonality of the Bessel function, into the following algebraic equation:

$$\begin{aligned}\frac{1}{32}a_{m-3,n}+\frac{3}{16}a_{m-2,n}+\frac{1}{2}\left(\frac{1}{\alpha^2}+\frac{15}{16}\right)a_{m-1,n}+\left(P_{mn}^2+\frac{1}{\alpha^2}+\frac{5}{8}\right)a_{mn}\\ +\frac{1}{2}\left(\frac{1}{\alpha^2}+\frac{15}{16}\right)a_{m+1,n}+\frac{3}{16}a_{m+2,n}+\frac{1}{32}a_{m+3,n}\\ =Q_{mn},\end{aligned} \tag{33}$$

where $P_{m,n}$ and $Q_{m,n}$ denote:

$$P_{mn}=\frac{2\lambda_n}{(2m-1)\alpha\pi\sqrt{\eta_0}}$$

and

$$Q_{mn}=\frac{48\eta_0 b_n}{\pi\sum_{n=1}^{\infty}\lambda_n b_n}\cdot\frac{(-1)^m}{(2m+3)(2m+1)(2m-3)(2m-5)} \tag{34}$$

Eq. (33) and the equations derived from Eq. (31) in the same procedure using $P_{m,n}$ and $Q_{m,n}$ form a system of linear equations with respect to $a_{1,n}, a_{2,n}, a_{3,n}, \cdots$. Any velocity distribution, $U(\eta)$ can be expanded in the form of (32), as long as $U(\eta_0)=0$ is satisfied, and then solutions of the linear equations give the following function of the electric current:

$$\psi(\xi,\eta)=\sum_m\sum_n\frac{4a_{mn}}{\alpha(2m-1)}\cos\frac{2m-1}{2}\pi\xi\sqrt{\frac{\eta}{\eta_0}}J_1\left(\lambda_n\sqrt{\frac{\eta}{\eta_0}}\right) \tag{35}$$

It is assumed here that the velocity distribution is given by $n=1$ in the form:

$$U(\eta)=\frac{2}{\lambda_1}\sqrt{\frac{\eta_0}{\eta}}J_1\left(\lambda_1\sqrt{\frac{\eta}{\eta_0}}\right) \tag{36}$$

Then dropping the subscript n, a system of linear equations is given in the following from:

$$\left(P_1^2+\frac{1}{2\alpha^2}+\frac{5}{32}\right)a_1+\frac{1}{2}\left(\frac{1}{\alpha^2}+\frac{9}{16}\right)a_2+\frac{5}{32}a_3+\frac{1}{32}a_4=Q_1,$$
$$\frac{1}{2}\left(\frac{1}{\alpha^2}+\frac{9}{16}\right)a_1+\left(P_2^2+\frac{1}{\alpha^2}+\frac{19}{32}\right)a_2+\frac{1}{2}\left(\frac{1}{\alpha^2}+\frac{11}{16}\right)a_3+\frac{1}{32}a_4=Q_2,$$
$$\frac{5}{32}a_1+\frac{1}{2}\left(\frac{1}{\alpha^2}+\frac{15}{16}\right)a_2+\left(P_3^2+\frac{1}{\alpha^2}+\frac{5}{8}\right)a_3+\frac{1}{2}\left(\frac{1}{\alpha^2}+\frac{41}{16}\right)a_4+\frac{1}{32}a_5=Q_3,$$

and for $m \geq 4$:

$$\frac{1}{32}a_{m-3}+\frac{3}{16}a_{m-2}+\frac{1}{2}\left(\frac{1}{\alpha^2}+\frac{15}{16}\right)a_{m-1}+\left(P_m^2+\frac{1}{\alpha^2}+\frac{5}{8}\right)a_m$$
$$+\frac{1}{2}\left(\frac{1}{\alpha^2}+\frac{15}{16}\right)a_{m+1}+\frac{3}{16}a_{m+2}+\frac{1}{32}a_{m+3}=Q_m, \tag{37}$$

where

$$P_m=\frac{2\lambda_1}{(2m-1)\alpha\pi\sqrt{\eta_0}},$$
$$Q_m=\frac{48\eta_0}{\pi\lambda_1}\frac{(-1)^m}{(2m+3(2m+1)(2m-3)(2m-5)}. \tag{38}$$

As is obvious from Eq. (38), Q_m is of the order of m^{-4}. When m is large, a_m is expected to be small. Thus the convergence of series in Eq. (35) is expected.

The numerical calculation was made of Eqs. (37) for various sets of α, the electron Hall parameter and $\sqrt{\eta_0}$, the parameter defining the width of the flow, using an electronic computer HITAC 5020F. In the first step of calculation, equation (37) was solved with the sweep-out method for an appriate value of m. Then, the solutions for $m+1$ were obtained with the same method. The comparison was made between coefficients $a_1, \cdots, a_m$ and $a_1', \cdots, a_m', a_{m+1}'$. The agreement between a_k and a_k' was satisfactory for k less than about $0.8m$ and the summation of Eq. (35) was calculated up to k. Then the solutions for $m+2$ were obtained and the summation was made up to $k+1$. The increase of m was stepped when the summation was no longer affected by the addition of higher term. Finally, the solutions were obtained for $m=100$ and the summation was made up to 80.

The stream function of the electric current is derived form Eq. (35):

$$\psi(\xi,\eta)=\left[\sum_{m=1}^{80}\frac{4a_m}{\alpha(2m-1)}\cos\frac{2m-1}{2}\pi\xi\right]\sqrt{\frac{\eta}{\eta_0}}J_1\left(\lambda_1\sqrt{\frac{\eta}{\eta_0}}\right)$$
$$=f(\xi)g\left(\frac{\eta}{\eta_0}\right). \tag{39}$$

In Fig. 36 the axial distribution of the summation f is shown for various of α. The radial distribution, g is shown in Fig. 37 together with that of U, given by Eq. (36). The resulting stream line of the Hall current is shown in Fig. 38.

The Hall current and the potential are derived from Eq. (20) using ψ, in the following:

$$J_x=\frac{1}{r}\left(\frac{\partial\xi}{\partial r}\frac{\partial\psi}{\partial\xi}+\frac{\partial\eta}{\partial r}\frac{\partial\psi}{\partial\eta}\right), \tag{40.1}$$

$$J_r=-\frac{1}{2}\left(\frac{\partial\xi}{\partial x}\frac{\partial\psi}{\partial\xi}+\frac{\partial\eta}{\partial x}\frac{\partial\psi}{\partial\eta}\right), \tag{40.2}$$

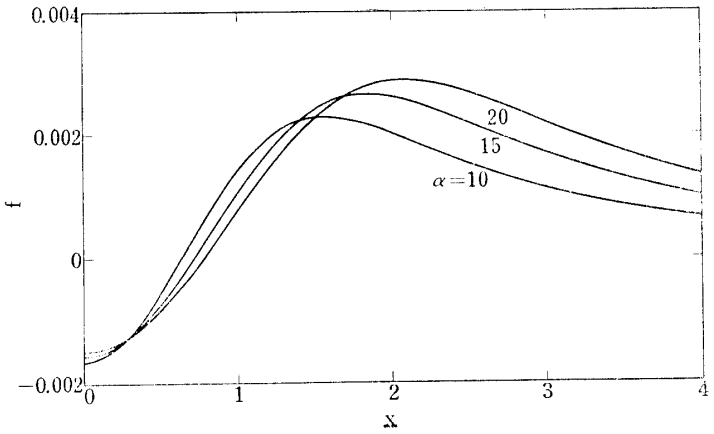

FIG. 36. Axial distribution of stream function of Hall current.

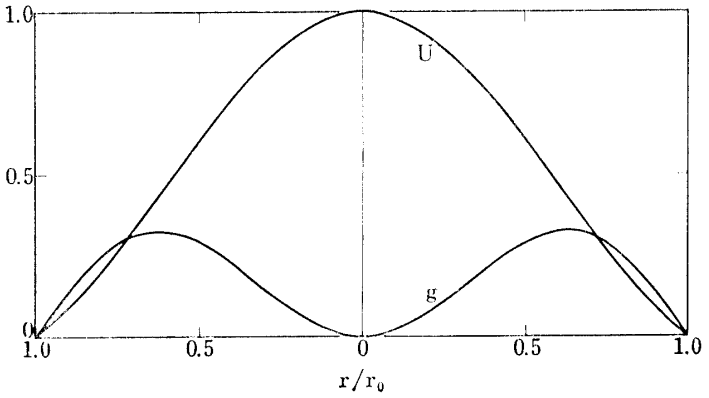

FIG. 37. Radial distribution of velocity and stream function of Hall current.

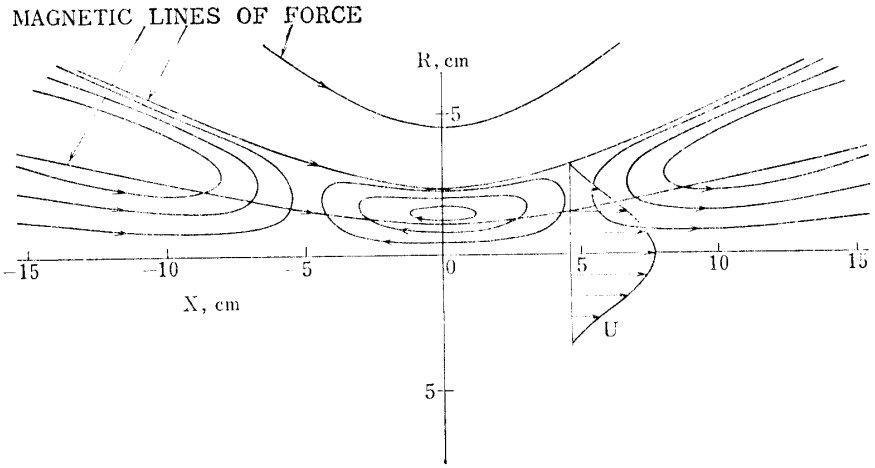

FIG. 38. Flow pattern of Hall current at $\alpha=10$.

$$J_\theta = UB_r - \frac{\alpha B^2}{r}\frac{\partial \psi}{\partial \xi}, \tag{40.3}$$

and

$$\frac{\partial \Phi}{\partial \xi} = -\frac{\partial \psi}{\partial \eta} \tag{40.4}$$

respectively. There equations with Eq. (39) being substituted reduce to the following equations:

$$J_x(\xi,\eta)=\frac{\lambda_1}{4\eta_0}\sum_{m=1}^{80}C_m\cos\frac{2m-1}{2}\pi\xi(1+\cos\pi\xi)J_0\left(\lambda_1\sqrt{\frac{\eta}{\eta_0}}\right), \tag{41.1}$$

$$J_r(\xi,\eta)=\frac{\pi(1+\cos\pi\xi)^{3/2}}{8\sqrt{\eta_0}}\sum_{m=1}^{80}C_m(2m-1)\sin\frac{2m-1}{2}\pi\xi\cdot J_1\left(\lambda_1\sqrt{\frac{\eta}{\eta_0}}\right)$$
$$+\frac{\pi\lambda_1\sin\pi\xi(1+\cos\pi\xi)^{1/2}}{8\sqrt{\eta_0}}\sum_{m=1}^{80}C_m\cos\frac{2m-1}{2}\pi\xi\sqrt{\frac{\eta}{\eta_0}}J_0\left(\lambda_0\sqrt{\frac{\eta}{\eta_0}}\right), \tag{41.2}$$

$$J_\theta(\xi,\eta)=\frac{\pi(1+\cos\pi\xi)^{1/2}}{2}\left[\frac{\sqrt{\eta_0}}{\lambda_1}\sin\pi\xi+\frac{\alpha}{8\sqrt{\eta_0}}(1+\cos\pi\xi)^2\sum_{m=1}^{80}C_m(2m-1)\right.$$
$$\left.\times\sin\frac{2m-1}{2}\pi\xi\right]J_1\left(\lambda_1\sqrt{\frac{\eta}{\eta_0}}\right) \tag{41.3}$$

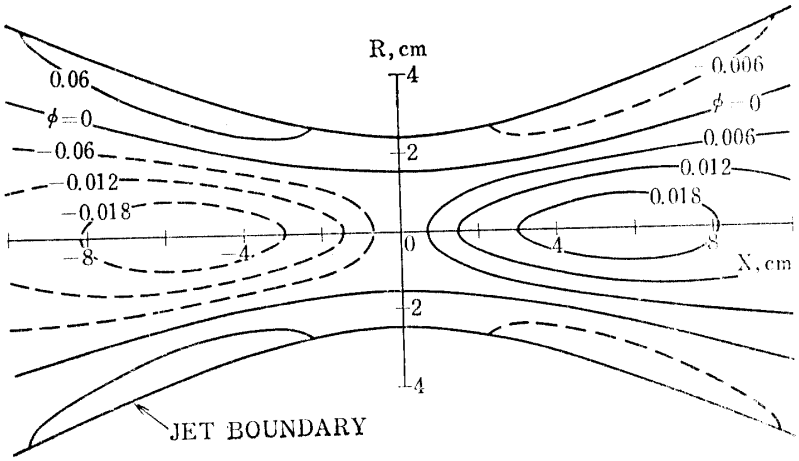

a) THEORETICAL, $\alpha=10$

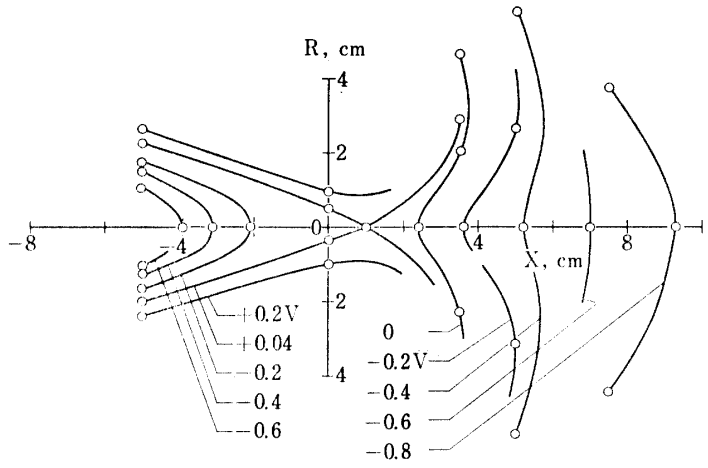

b) EXPERIMENTAL, $\dot{m}=0.15$g/sec

FIG. 39. Equipotential lines;
a) Theoretical result for $\alpha=10$. ϕ represents nondimensional potential.
b) Experimental results, $\dot{m}=0.15$ g/sec and $B_0=1000\,G$.

and

$$\Phi(\xi,\eta)=-\frac{\lambda_1}{\pi\eta_0}\sum_{m=1}^{80}\frac{C_m}{2m-1}\sin\frac{2m-1}{2}\pi\xi\cdot J_0\left(\lambda_1\sqrt{\frac{\eta}{\eta_0}}\right), \qquad (41.4)$$

where

$$C_m=\frac{4a_m}{\alpha(2m-1)}. \qquad (42)$$

The equipotentials are shown in Fig. 39. The results of the above calculation are compared in the following chapter with the the experimental results obtained in Chapter IV.

VI. Discussion

The experimental results of Chapter IV are discussed in the light of the theoretical analysis in Chapter V. The experimentally obtained distributions are compared in Section 1 with the results of the numerical calculation shown in the preceding chapter.

The perturbation of the velocity field by the electromagnetic effects is discussed qualitatively in Section 2.

VI-1. *Hall Potential*

From the experimental condition of $\omega_e\tau_e$ of more than 10 and negligibly small $\omega_i\tau_i$, it is obvious that electrons gyrate closely around the magnetic lines of force and that ions are hardly affected by the magnetic field. As a result there arises a weak charge separation because ions tend to remain on their path being unaffected by the magnetic field. Then the induced electric field is radially inward in the upstream region of the coil where the magnetic field converges and radially outward in the downstream where the magnetic field diverges. Near the center of the coil the magnetic lines of force are almost parallel to the flow. Therefore, the interaction of the charged particles with the magnetic field is weak and no electromotive force is generated in this region.

To sum up the above considerations, the Hall potential on the centerline becomes minimum in the upstream region of the coil where B_r/r is nearly minimum, and the situation reverses downstream of the coil. The strong radial electric field directs towards the axis in the upstream region and outwards from the axis in the downstream. The electric current on the centerline is driven by the potential gradient mentioned above and flows towards upstream near the coil center.

In Fig. 40 is shown the comparison between the experimental and the theoretical distributions of the potential on the centerline. The experimental results are obtained at flow rates of 0.15 and 0.06 g/sec. The Hall parameters of electron are 11 and 33, respectively difference of the floating potential from

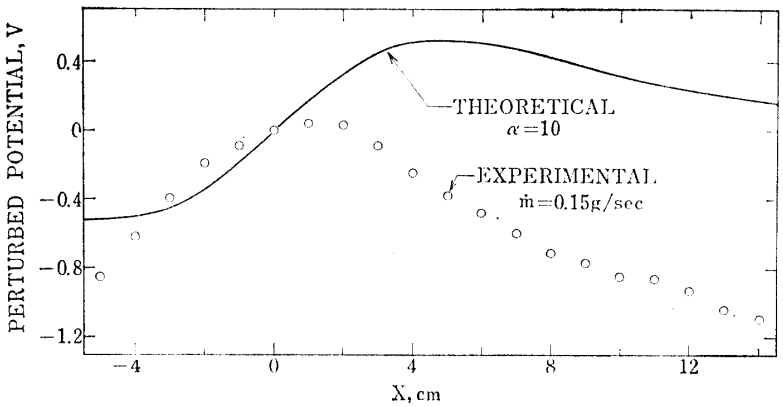

FIG. 40. Axial distribution of measured and calculated perturbed-potential.

the value at X=0, the center of the coil, is plotted against the axial position. As has been shown in Fig. 14, the potential distribution without the magnetic field originates mostly from the ambipolar diffusion. The axial electric fields are, as shown in Figs. 28 and 29 with open circles, very weak. When the magnetic field is applied, the ambipolar diffusion does not contribute strongly to the potential distribution although it is difficult to separate the Hall effect and the effect of the magnetic field on the ambipolar diffusion. Therefore, the potential distribution when there is no interaction has been assumed to be uniform. The theoretical values are obtained for the sets of $\alpha=10$, $\sqrt{\eta_0}=0.22$ to match the experimental conditions of $\dot{m}=0.15$ g/sec. The theoretical curves are obtained using $U_\infty=1.8$ km/sec for $\dot{m}=0.15$ g/sec, $B_0=1000$ gauss of magnetic field and $L=7.75$ cm.

The radial distribution of perturbed potential is compared in Fig. 41 for $\dot{m}=0.15$ g/sec. The good agreement is found upstream of the coil. The radial

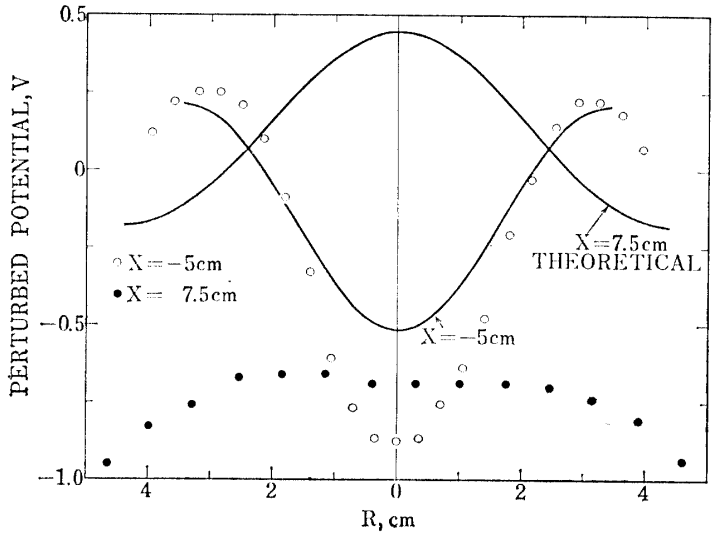

FIG. 41. Radial distribution of measured and calculated perturbed-potential.

distribution shows a valley of potential on the centerline at X=−5 cm and a peak at X=7.5 cm, as has been explained from the consideration of electron motions in the magnetic field. The experimental distribution at X=7.5 cm is not in agreement with the theoretical result.

In Fig. 39 the experimentally obtained equipotential lines are compared with theoretical ones. An excellent similarity is demonstrated upstream of the coil, whereas the similarity cannot be found downstream. Upstream of the coil a strong electromagnetic interaction takes place between the slightly expanding flow and the magnetic field with converging lines of force. Once the flow is aligned with the lines of force, the interaction between the flow and the magnetic field disappears and the electrostatic effects become dominant. Consequently, the theoretical equipotentials based on electromagnetic interaction are similar to the experimental results only upstream of the coil.

VI-2. *Perturbation of the Flow Field*

The velocity distributions on the centerline obtained with the magnetic field, shown in Figs. 31 and 32 are similar to the supersonic flow through a solid nozzle, where the flow is decelerated at the converging region and is accelerated at the diverging region.

The axial variation of the half-value radius of the saturation ion current shown in Fig. 26 illustrates a similar trend. The boundary of the flow is deformed into a converging-diverging shape closely along the magnetic lines of force. The diameter of the jet becomes the minimum at the position of the coil, X=0, and increases downstream.

When the interaction is weak, the perturbation of the flow velocity by the application of the manetic field is explained theoretically by Eq. (15). If the mean velocity has only an axial component, and as the azimuthal component of magnetic field is zero, Eq. (15) is resolved into the following components;

$$U\frac{\partial u}{\partial x}+\frac{\partial p}{\partial x}=J_\theta B_r, \tag{43}$$

$$U\frac{\partial v}{\partial x}+\frac{\partial p}{\partial r}=J_\theta B_x. \tag{44}$$

The applicability of Eqs. (43) and (44) is limited by the linearization process with respect to the interaction parameter, ε. Furthermore the velocity distribution, $U(r)$ is not known experimentally. Therefore, even if the solution were to be calculated, they have no meanings more than the qualitative consideration which follows below. The right-hand sides of Eqs. (43) and (44) represent the Lorentz force, of which the distributions obtained from the theoretical results in Chapter V are shown in Fig. 42. The axial component of the body force, shown in Fig. 42-a is symmetric with respect to the plane of X=0, and acts always as a drag. The distribution of the drag near the centerline behaves as r^2. The radial component, on the other hand, is anti-symmetric with respect

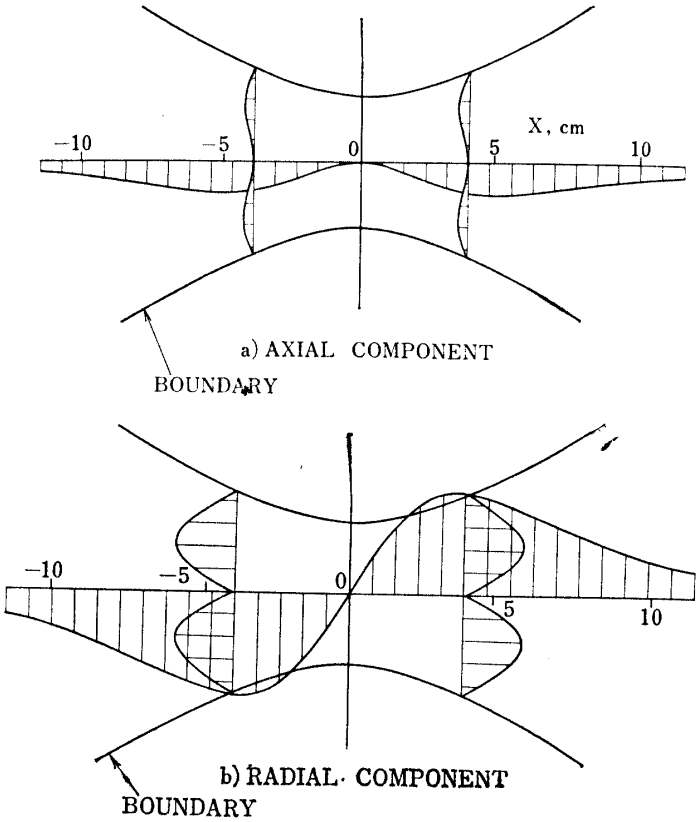

FIG. 42. Distribution of Lorentz force.

to X=0, as is shown in Fig. 42-b. In the upstream side of the coil, the force acts to pinch the flow. In the downstream the force changes its sign and acts to expand the flow. The radial force is proportional to r near the centerline. Therefore the radial component of the body force is to override the axial one because the rather slender jet is now in concern. Then the deformation of the boundary of the jet is understood to be the result of the interaction between the induced current J_θ and axial component of the magnetic field.

The plasma flow of the present experiment with the Mach number of about 2 is decelerated in the upstream side of the coil, where the radial force acts to decrease the cross-sectional areas. In the downstream, the radial force acts to widen the radius and the velocity increases. As a result, the axial velocity reaches the maximum at about X=5 cm.

A simple estimation can be made on the flow quantities if the flow is isentropic and its boundary coincides with the magnetic lines of force. The lowest curve in Fig. 43 shows the isentropically expanded velocity. Comparison with the experimental value shows obviously that the magnetic nozzle has the additional mechanism of acceleration to that of a simple solid nozzle flow. Electrostatic acceleration of ions by electrons of high temperature and expansion of ions heated by Joule dissipation are proposed to account for the high exhaust velocity of ions.

The acceleration of electrons in the magnetic field with diverging field lines

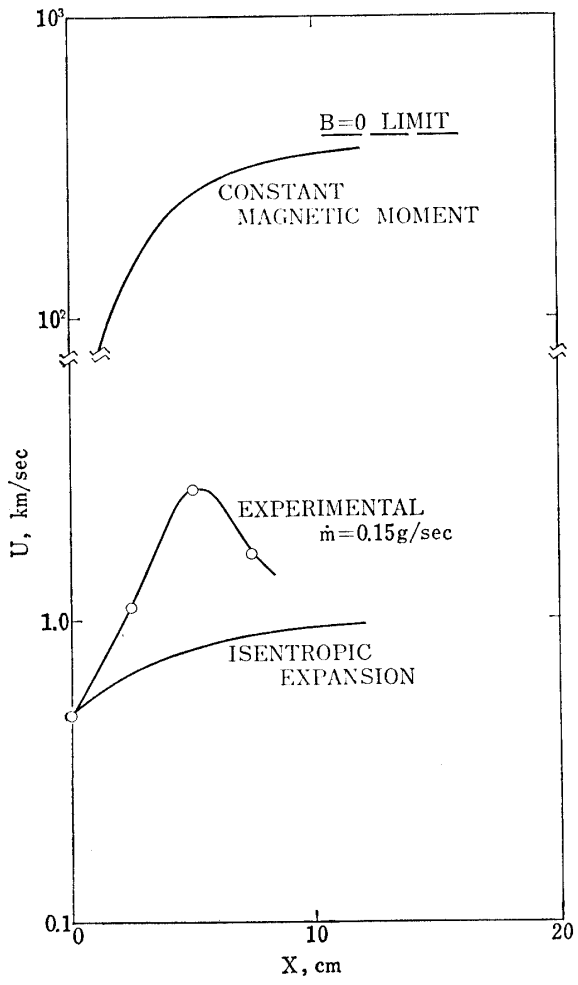

FIG. 43. Axial distribution of velocity.

can be calculated if a constant magnetic moment [1] is assumed. The concept means that the thermal motion of electrons perpendicular to the magnetic field is transformed into the axial motion along the diverging magnetic field. The uppermost curve in Fig 43 shows the result of the calculation. At $X=5$ cm where the axial component of the magnetic field is 591 gauss on the centerline, the electrons acquire the velocity of about 260 km/sec. This is about a hundered times the experimental result of the ion velocity. This high velocity is not realized because the calculated velocity of electrons has been obtained without considering the deceleration caused by the ions. Ions are not affected by the magnetic field because of their small gyration frequency. They are accelerated by electrons through the electrostatic force. The electrostatic effect is clarly demonstrated in Fig. 39b and seems to be one of the important mechanism of the accelation in the magnetic nozzle. Electromagnetic compression and Joule heating result in the increase of luminosity and electron temperature at $X=0$ as has been shown in Figs. 21 and 27.

The electric-current density at the center of the coil is estimated to be of the order of 1 ampere/cm^2. It is assumed here that the energy dissipated by the Hall current is totally transfered into the thermal energy of electrons as a Joule heating and that the thermal energy of electrons is transferred into the kinetic energy of ions in the diverging section of the magnetic nozzle. The resulting axial velocity of ions becomes about 1.5 km/sec. Together with the aerodynamic effects, the velocity of 2.6 km/sec is estimated. The value is consistent with experimental results. The neutral argon atoms can reach only 200 m/sec if both ions and atoms equally obtain the axial kinetic energy. As has been concluded from the measurement of an impact pressure in Chapter IV, the neutral particles are almost unaffected by the magnetic field. The mean-free-path of successive collisions of ions with neutral atoms is estimated to be about twenty times that with electrons. Therefore the assumption that only the ions are electrostatically accelerated is justified.

Then the mechanism of the interaction is summerized in the following. The electrons in the first place obtain the kinetic energy transforming their thermal energy by the aid of the magnetic field. Then ions are accelerated by the electric field thus induced and also transforming the thermal energy obtained through the collisions with electrons, into the kinetic energy. The neutral particles act as the momentum source to promote the Lorentz interaction upstream of the coil. The energy thus deprived from the neutral particles is transferred to the electrons by the Joule heating. At $X>5$ cm, the viscous force overrides.

The neutral atoms spend their kinetic energy in driving an electric current, i.e. Joule heating. This takes place mostly in the converging section of the magnetic nozzle. In the diverging section, heated ions and electrons expand and are accelerated. Thereby the electrons deliver a part of their thermal energy for ion acceleration.

Conclusion

Conclusions of the present investigation on the plasma flow through a magnetic nozzle when the Hall parameter is larger than unity, is summarized as follows:

1. An ionized gas flow with a large electron Hall parameter is produced in a vacuum tank with a dc arc discharge. The ion number density and the electron temperature are about $1\times10^{13}\,\mathrm{cm}^{-3}$ and 5000°K, respectively. An electron Hall parameter ranges from 10 to 30.

2. By the application of the magnetic field there result three influences on the flow. First, the flow is strongly pinched. The diameter of the jet becomes about half of that without the magnetic field. Second, an electric field of about 0.1 V/cm is induced. The electric field directs upstream i.e. has negative sign near the coil center. The third of them is the effect on the flow velocity. The flow is decelerated in the upstream region and accelerated in the downstream region.

3. The flow boundary is deformed into a converging-diverging contour and the path of charged particles lie closely on the magnetic line of force.

4. The electric field is induced due to the charge separation between gyrating electrons and heavy ions. The result of the theoretical analysis based on the generalized Ohm's law is in the quantitative agreement with the experimental results upstream of the coil.

5. The body force obtained theoretically has a component to pinch the flow in the upstream region and to expand in the downstream region of the coil. The experimental results on the deformation of the flow boundary and the perturbation on the flow velocity are explained qualitatively by the theoretical distribution of body force. The velocity in the diverging region of the magnetic nozzle is higher than the value estimated from the isentropic expansion.

6. The acceleration process in the magnetic nozzle is explained by the magnetic pumping action and the electrostatic force. In the upstream region the

magnetic pumping action is dominant. An interaction of the induced current with the magnetic nozzle causes the pumping force and deforms the boundary. In the downstream region the electrostatic force dominates. The acceleration of electrons along the magnetic lines of force cause the charge separation and ions are accelerated. The directional energy of ions is supplied from the thermal energy of electrons which is acquired as the Joule heat in the magnetic nozzle in addition to the initial thermal energy.

Acknowledgement

The authors wish to express their gratitudes of Professor H. Sato for his continuous encouragements and valuable suggestions throughout the work. Thanks are extended to Professor H. Hasimoto for discussions on the theoretical analysis.

Department of Aerodynamics
Institute of Space and Aeronautical Science,
University of Tokyo, Tokyo
October 20, 1970

References

[1] Spitzer, L. Jr., Physics of Fully Ionized Gases, Interscience Publishers, (1962).
[2] Kosmahl, H. G., NASA TN D-3782, (1967), also J. Appl. Phys. **38**, 4576, (1968).
[3] Hasimoto, H., J. Phys. Soc. of Japan **19**, 1457, (1964).
[4] Otis, D. R., Report No. AS-64-1, Institute of Engineering Research, University of California, (1964), also, J. Fluid Mech. **24**, 41, (1966).
[5] Clark, K. E. & Jahn, R. C., Astronautica Acta **13**, 315, (1967).
[6] Laframboise, J., Univ. of Toronto, Institute of Aerospace Studies, Report No. 100, (1965).
[7] Chen, F. F., *Plasma Diagnostic Techniques,* edited by R. H. Huddlestone and S. L. Leonard (Academic, New York, 1965), p. 113.
[8] Adcock, B. D. & Plumtree, W. E. G., Aeronautical Research Council Current Papers, C. P. No. 701, (1965).
[9] Olsen, H. N., J. Quant. Spectro. Red. Transfer, **3**, 59, (1963).
[10] Johnson, R. A., McClure, B. T. & Holt, R. B., Phys. Rev. **80**, 376, (1950).
[11] Bailey, A. B. & Boylan, D. E., Proc. of the 1962 Heat Transfer & Fluid Mechanics Institute (1962), p. 62.
[12] Ashkenas, H. & Sherman, F. S. Proc. of the 4th Int. Symp. on Rarefied Gas Dynamics (1966), p. 84.